EDGE ARTICLE

Check for updates

Revealing the exchange kinetics of thiol-capped Au₂₅ nanoclusters with alkynyl ligands

Yuping Chen,†[a] Guoqing Bian,†[b] Zhikun Wu [ID] *[b] and Qing Tang [ID] *[a]

Ligand exchange is an important strategy to functionalize metal nanoclusters (NCs) for enhanced properties. Thiolates and alkynyls have been widely used for NC protection; however, the possibility for alkynyl-for-thiolate exchange as well as the kinetics for the ligand exchange process have remained largely unexplored. Herein, we have reported for the first time a kinetic investigation into the alkynyl-for-thiolate exchange through the reaction of thiolated $Au_{25}(SR)_{18}$ with the incoming alkynyl ligands. Interestingly, our simulations revealed the electronic and steric effects of alkynyl ligands and the precursor cluster's charge state collectively govern the exchange efficiency and regioselectivity. Notably, the alkynyl-for-thiolate exchange is highly facile when reacting with the nucleophilic lithium or gold(I)−alkynyl complex ($Au(C\equiv CR)$ or $Li(C\equiv CR)$), but fails when using $HC\equiv CR$ as the exchange ligand. The $Au(C\equiv CPh)$ complex exhibits charge-state-dependent exchange at the S_1 or S_2 position, whereas the sterically bulky $Au(C\equiv C^tBu)$ complex decelerates the exchange kinetics and universally targets the S_1 position as the exchange product. By contrast, the lithium−alkynyl complex ($Li(C\equiv CPh)$ or $Li(C\equiv C^tBu)$) preferentially leads to the S_1' exchange isomer, driven by the ionic Li−C bonding that enhances the $C\equiv C$ π^*-electron density and alkynyl nucleophilicity. Our predictions are further validated by the ligand exchange experiments between phenyl ethanethiol (PET) protected $[Au_{25}(PET)_{18}]^-$ and $Au(C\equiv C^tBu)$. The electrospray ionization mass spectra (ESI-MS) unambiguously confirm the successful substitution of 4, 5 and 6 PET ligands by the $-C\equiv C^tBu$ ligand, and the absorption spectrum drastically changes upon alkynyl exchange. This work establishes an important atomic-level understanding of the alkynyl-for-thiolate exchange mechanism, offering a convenient strategy for realizing alkynyl and thiolate co-protected gold clusters under mild conditions.

Introduction

Atomically precise gold nanoclusters (Au NCs) protected by organic ligands have emerged as a central focus in nanomaterials research due to their well-defined atomic structures, unique physicochemical properties and tunable reactivity.[1–4] These properties are highly sensitive to factors such as the cluster size, shape, the metal–ligand interface, and the ligand environment, making Au NCs ideal candidates for various tailored applications.[5,6] By rationally modifying the core and surface or interface structures, the electronic and catalytic properties of Au NCs can be fine-tuned to the optimal level. In this context, the protecting ligands play a dual role, which on one hand, stabilize the cluster framework from agglomeration,

while on the other hand, modulate the interface properties and coordination environment of the metal active sites.[4] In particular, as a powerful post-synthesis strategy, ligand exchange provides a versatile tool for the modification and functionalization of metal NCs.[7–10] This technique has been widely applied to enhance the cluster properties such as photoemission,[11,12] chirality,[13–15] and solubility,[16–19] thereby expanding the potential applications of Au NCs in fields ranging from biomedicine[20,21] to nanocatalysis[22] to cluster self-assembly.[23] In terms of ligand exchange, recent efforts have mainly concentrated on the exchange reaction of thiolate-protected gold NCs with free thiol or thiolated metal complexes,[24–27] wherein some of the surface ligands are replaced with new thiolate ligands to control the surface chemical functionalization of Au NCs.[9,28–31] It has been demonstrated that the thiol exchange reaction is enabled by the flexibility and reactivity of the Au–S interface, in which the ligand-exchange position and kinetics are largely controlled by the electronic and steric effects of the incoming thiol ligands.

In addition to the widely studied thiolate (–SR) ligands, the alkynyl ligands (–C≡CR) have recently emerged as new alternatives for surface functionalization, and have gained special attention for their ability to interact with gold through

[a]*School of Chemistry and Chemical Engineering, Chongqing Key Laboratory of Chemical Theory and Mechanism, Chongqing University, Chongqing 401331, China. E-mail: qingtang@cqu.edu.cn*

[b]*Key Laboratory of Materials Physics, Anhui Key Laboratory of Nanomaterials and Nanotechnology, CAS Center for Excellence in Nanoscience, Institute of Solid State Physics, Chinese Academy of Sciences, Hefei, Anhui 230031, China. E-mail: zkwu@issp.ac.cn*

† These two authors contributed equally to this work.

electronic conjugation as well as versatile interface interactions to form stable organogold nanoclusters.[32] These interactions offer new opportunities for tuning the electronic and catalytic properties of Au NCs. In 2011, Tsukuda *et al.* reported the first experimental synthesis of a series of homoleptic alkynyl-protected Au NCs by direct ligand exchange of preformed polyvinylpyrrolidone (PVP)-stabilized Au NCs with phenylacetylene (PhC≡CH)[33] under thermal conditions in a biphasic solvent system. Later in 2015, Konishi *et al.* introduced two alkynyl ligands on the surface of an icosahedral Au$_{13}$ skeleton ([Au$_{13}$(dppe)$_5$(C≡CPh)$_2$]$^{3+}$) by the ligand exchange reaction of a dichloro-substituted Au$_{13}$ cluster ([Au$_{13}$(dppe)$_5$Cl$_2$]$^{3+}$) with a free PhC≡CH ligand under basic conditions.[34] Besides the post-synthetic ligand exchange method, the alkynyl gold NCs are more often achieved by the bottom-up reduction of gold(I) alkynyl precursors in solution,[35] and thus far, more than two dozen alkynyl gold NCs with well-defined compositions and structures (*e.g.*, Au$_{19}$, Au$_{23}$, Au$_{24}$, Au$_{25}$, Au$_{36}$, Au$_{38}$, Au$_{44}$, and Au$_{144}$) have been prepared *via* the direct reduction route.[36] Among them, some alkynyl protected Au NCs even share the same structures and ligand-to-metal ratio as their thiolate protected counterparts. A representative example is Au$_{36}$(C≡CPh)$_{24}$ and Au$_{44}$(C≡CPh)$_{28}$, which are, respectively, isostructural to their thiolated Au$_{36}$(SR)$_{24}$ and Au$_{44}$(SR)$_{28}$ counterparts.[37] Another intriguing example is [Au$_{25}$(C≡CR)$_{18}$]$^-$,[38] which has the same icosahedral Au$_{13}$ core as in [Au$_{25}$(SR)$_{18}$]$^-$, but the peripheral six V-shaped dimeric staple motifs are arranged differently. Moreover, recent determination of the ligand effect in alkynyl *vs.* thiolate has demonstrated that the alkynyl-protected metal NCs exhibit better stability against oxidation and much enhanced catalytic performances in comparison with the thiolated counterparts.[39,40] This indicates that there might exist a similar but quite different parallel universe between the alkynyl-protected Au NCs and the thiolated ones.

In particular, the structural similarity between thiolate- and alkynyl-protected metal NCs suggests that the alkynyl ligands might possibly replace the thiolates in the protecting motifs *via* the ligand-exchange process. Noteworthily, the alkynyl and thiolate ligands have similar but different coordination preferences, both being negatively charged and forming strong interactions with the metals, but the thiolate usually adopts the σ-only coordination modes, whereas the alkynyl with its C≡C bond would coordinate with the metals *via* σ- or/and π-bonding modes. Their distinct metal–ligand interactions provide new avenues for controlling the cluster reactivity and stability, it thus would be highly desirable to realize the exchange reactions between alkynyl and thiolate ligands to produce potentially new properties in the atomically precise Au NCs.[32,36] However, the exchange of alkynyl for thiolate ligands is challenging, and thus far only a few studies have conducted the alkynyl-for-thiolate (or thiolate-for-alkynyl) exchange on Au NCs. In this context, the first attempt towards the alkynyl-for-thiolate exchange was reported in 2020 by the Ackerson group.[41] Their results revealed that the thiolate-protected Au NCs such as Au$_{25}$(SR)$_{18}$ can readily undergo the alkynyl-for-thiolate ligand exchange under mild conditions when a lithium–phenylacetylide or gold(I)–phenylacetylide complex was used as the incoming ligand.[41] They further showed that the reverse thiolate-for-alkynyl

exchange is also facile when using the free thiol as the incoming ligand to the alkynyl-protected Au$_{25}$(C≡CAr)$_{18}$ NCs. However, due to the possible large number of competing exchange products, the distribution of the reaction products is very complicated, and no specific composition with well-defined formulae or crystal structure was isolated successfully at that time. In a more recent report, Nakamura *et al.* has demonstrated that partial ligand exchange with alkynyl groups on Au$_{25}$(SR)$_{18}$ is crucial for enabling the dual catalytic activity,[42] which greatly promotes the photocatalytic cross-dehydrogenative coupling of terminal alkynes and tertiary amines. Despite the impressive progress, examples of alkynyl-for-thiolate exchange reactions or *vice versa* are, currently, still very rare, and the microscopic details of the exchange mechanism remain obscure. A molecular-level understanding of the transformation mechanism and the preferred reactive sites in the ligand exchange process will enable more precise engineering of surface microenvironments. Therefore, it is essential to clarify the alkynyl-for-thiolate exchange mechanism and develop strategies for controlling regioselectivity during this exchange process to design mixed-ligand metal NCs with new functionalities.

In this work, using the widely studied Au$_{25}$(SR)$_{18}$ as the parent cluster, we performed systematic first-principles simulations to probe the reactivity of phenyl ethanethiol (PET)-protected Au$_{25}$(PET)$_{18}$ with the alkynyl ligands (Scheme 1), including free phenylacetylene (PhC≡CH) and the alkynyl metal compounds (gold(I)–acetylide or lithium(I)–acetylide) as the incoming ligands. As shown in Scheme 1a, the protecting motif of Au$_{25}$(PET)$_{18}$ NC features an elegant assembly of six dimeric [RS–Au(I)–SR–Au(I)–SR] units around the icosahedral Au$_{13}$ core.[43] In this dimeric motif, one thiolate ligand is positioned at the apex (denoted as the "S$_2$" site), while two other thiolates are anchored to the surface of Au$_{13}$ core, which are differentiated by the different orientations of SR groups. The thiolate that orients in a *cis*-configuration with the apex SR is denoted as "S$_1$", while that orienting in a *trans*-configuration with the apex SR is denoted as "S$_1'$". This unique arrangement gives rise to three possible distinct regioisomers (S$_1$, S$_2$, and S$_1'$) in the ligand-exchanged products (Scheme 1b).

Based on the above Au$_{25}$(PET)$_{18}$ model cluster, we then pursued an atomic-scale mechanism governing the alkynyl-for-thiolate exchange efficiency and regioselectivity, focusing on the influence of ligand electronic characteristics, steric interactions and the charge state of Au$_{25}^q$ ($q = -1$, 0, and +1) NCs. The free energy calculations with enhanced sampling revealed the fundamental energy constraints (>3 eV) for the direct HC≡CR-for-thiolate exchange, a consequence of the highly localized and rigid C≡C π-bond causing mismatch with the cluster frontier orbitals. Notably, the alkynyl–metal complexes (*e.g.*, Au/Li(C≡CPh)) overcome these constraints and initiate the exchange reactions through the π-system polarization. The Au(C≡CPh) species characterized by the d–π* back-bonding between the occupied Au d orbitals and the π* orbitals of the C≡C bond exhibits charge-state-dependent regioselectivity, in which the negatively charged [Au$_{25}$(SR)$_{18}$]$^-$ favors the S$_1$ isomer formation, while the neutral Au$_{25}$(SR)$_{18}$ promotes the selective
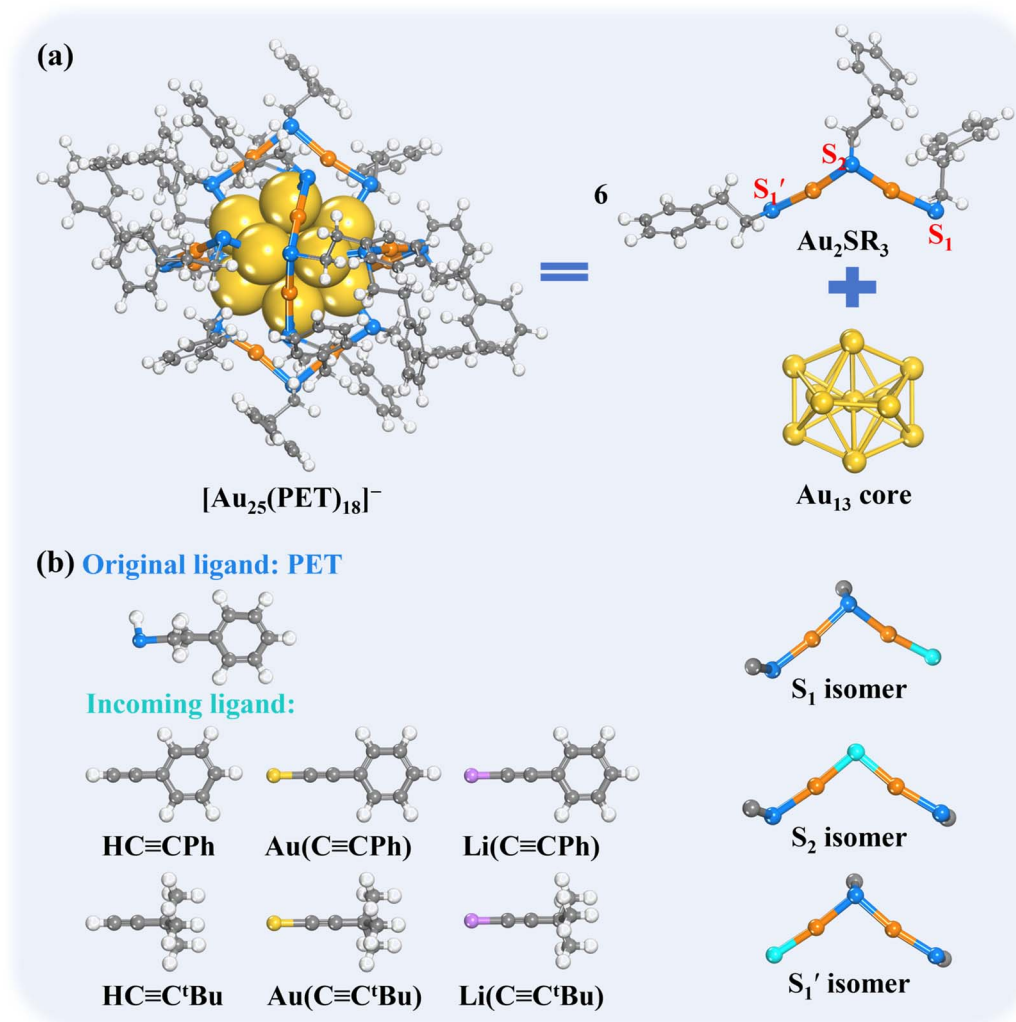
Scheme 1 (a) Structure of $[Au_{25}(PET)_{18}]^-$ and three possible exchange sites in the ligand-exchange reaction. (b) The original PET ligand and the incoming alkynyl ligand, including HC≡CPh, Au(C≡CPh), Li(C≡CPh), HC≡C^{t}Bu, Au(C≡C^{t}Bu) and Li(C≡C^{t}Bu), as well as the three possible regioisomers formed after the ligand-exchange reaction (the site of the exchanged alkynyl ligand is colored in green). Color code: core Au – yellow (Au$_{25}$ cluster); staple Au – orange (Au$_{25}$ cluster); S – blue; C – gray; incoming ligand – sapphire; Li – purple; H – white.

substitution at the apex S_2 site. Differently, the bulkier Au(C≡C^{t}Bu) universally targets the S_1 position across the different charge states, wherein the bulkier *tert*-butyl ligand slows down the exchange kinetics relative to the phenyl analogues (–C≡CPh) while thermodynamically stabilizing the exchange products. By comparison, the Li-coordinated alkynyl complexes (Li(C≡CR)) universally generate the S_1' isomers, driven by the ionic Li–C bonding that enhances the C≡C π*-electron density. Importantly, the Au center in Au(C≡CR) actively participates in the exchange, whereas the Li center in Li(C≡CR) functions solely as a transient mediator. This non-incorporative mediation promotes ligand exchange without inducing significant Au$_{25}$ structural reorganization. Our predictions are further validated by the ligand exchange experiments. The electrospray ionization mass spectrum (ESI-MS) quantification confirms the replacement of 4, 5 and 6 PET ligands by –C≡C^{t}Bu on $[Au_{25}(PET)_{18}]^-$. These insights

establish clear mechanistic guidelines for the atom-precise alkynyl-for-thiolate engineering of Au$_{25}$(PET)$_{18}$ clusters, signifying the importance of electronic and steric effects as well as the precursor charge states in collectively dictating the substitution pathways.

Methods

Computational modeling

The $[Au_{25}(PET)_{18}]^q$ ($q = -1, 0, +1$) NCs were initially placed within a cubic simulation box measuring 30 Å × 30 Å × 30 Å, followed by optimization to obtain the most stable configuration. To simulate the ligand exchange process with varying alkynyl ligand (*e.g.*, HC≡CPh) concentrations at 10 or 40 equivalents, 10 or 40 alkynyl ligand molecules were incorporated around the $[Au_{25}(PET)_{18}]^q$ cluster during the unconstrained molecular dynamics (MD) simulations. This setup

allowed for the exploration of ligand exchange dynamics at different ligand concentrations. For the constrained MD simulations and free energy calculations, only a single alkynyl ligand was incorporated around the cluster to model the exchange of the specific PET ligand at the designated position.

DFT calculations

The *ab initio* molecular dynamics (AIMD) simulations and constrained MD (c-MD) simulations were performed using the CP2K package (version 2023),[44] based on the PBE functional and a hybrid Gaussian/Plane-Wave scheme (GPW).[45] The GTH pseudopotentials were chosen to describe the core electrons. The wave functions were expanded in optimized double-ζ Gaussian basis sets, and the plane waves were expanded with a cutoff energy of 400 Rydberg.[46] Dispersion correction was applied in all calculations with the DFT-D3(BJ) method.[47] The simulations were sampled by the canonical (*NVT*) ensemble employing Nose–Hoover thermostats with a time step of 1.0 fs at a finite temperature of 298.15 K for more than 10 ps.[48] Constrained molecular dynamics (c-MD) simulations were calculated based on the thermodynamic integration (TI) method,[49,50] where the reaction free energy and kinetic barrier were obtained by applying a holonomic constraint on the reaction coordinate (ζ) during MD simulations and integrating over the average unbiased force associated with the reaction coordinate, as shown in the following equation:

$$\Delta A(\zeta_a, \ \zeta_b) = -\int_{\zeta_a}^{\zeta_b} \frac{dF(\zeta)}{d(\zeta)} d\zeta,$$

where $\Delta A(\zeta_a, \ \zeta_b)$ is the free energy difference between two reaction coordinates (ζ_a and ζ_b) and $F(\zeta)$ is the averaged constrained force. ζ is the velocity of transformation, and the free energy gradient $\frac{dF(\zeta)}{d\zeta}$ can be computed along c-MD using the SHAKE algorithm.[50] The growth speed ($d\zeta$) was set as 0.0008, and the tolerance for the Shake/Rattle constraint algorithm was set as 0.0001. The reaction barriers were obtained by integrating the free-energy gradients to compute the free energy profiles based on thermodynamic integrations.

Molecular fragment calculations

The molecular fragments were modeled using the Gaussian 16 software package.[51] Geometry optimizations were performed with the B3LYP functional, employing the 6-31G(d) basis set for Li, C, N, and H atoms[52] and the Stuttgart/Dresden (SDD) effective core potential for the Au atom.[53] To account for the dispersion interactions, the D3 correction with Becke–Johnson damping was applied.[54] Molecular orbital analysis, Hirshfeld/CM5 population analysis, and Mayer bond order analysis[55–57] were carried out using the Multiwfn program,[58] based on the converged wavefunctions obtained from the DFT calculations.

Experimental section

Chemicals

All chemicals are commercially available and were used as received. Tetrachloroauric(III) acid (HAuCl$_4$·4H$_2$O, >99.8%), triethylamine (Net$_3$, ≥99.5%) and sodium borohydride (NaBH$_4$, 99.8%) were purchased from Shanghai Chemical Reagent Co., Ltd. Tetraoctylammonium bromide (TOAB, ≥98.0%), dimethyl sulfide (DMS, ≥99%) and 3,3-dimethyl-1-butyne ((CH$_3$)$_3$-CC≡CH, ≥98.0%) were purchased from Aladdin. Solvents dichloromethane (DCM), dimethyl sulfoxide (DMSO), petroleum ether, tetrahydrofuran, toluene, acetone and methanol were purchased from Shanghai Chemical Reagent Co., Ltd. The water used in all experiments was ultrapure (resistivity: 18.2 MΩ cm), produced using a Milli-Q NANO pure water system. Me$_2$SAuCl was prepared according to the literature methods.[59]

ESI-MS data collection

Electrospray ionization (ESI) mass spectra were recorded on a Waters Q-TOF mass spectrometer using a Z-spray source. The sample was first dissolved in toluene (~0.5 g L^{-1}) and then diluted (6/1 v/v) with a dimethyl sulfoxide (DMSO) solution containing 50 mmol of CsOAc. The sample was directly infused into the chamber at 5 μL min^{-1}. The source temperature was maintained at 70 °C, the spray voltage was 2.20 kV and the cone voltage was adjusted to 60 V.

Synthesis of TOA[Au$_{25}$(PET)$_{18}$]

A previously published method was adapted for the synthesis of TOA[Au$_{25}$(PET)$_{18}$].[60] Specifically, in a 100 mL three-necked flask, 674.8 mg of TOAB and 30 mL of tetrahydrofuran solution were added and rapidly stirred for 10 minutes. Then, 500 mg of HAuCl$_4$·4H$_2$O was added to the solution. After stirring at medium speed for 30 minutes, the solution changed from yellow to burgundy. Afterwards, 1020 μL of PET was added to the solution, and the stirring was continued at a low speed for 4 hours. The solution gradually changed to colorless. The flask was placed in an ice bath and stirred rapidly for 17 hours after adding 528.2 mg of aqueous NaBH$_4$. The solution was washed three times with methanol and centrifuged. The resulting precipitate was dissolved in 8 mL of toluene and mixed with 32 mL of methanol in a 50 mL beaker. After one day, a large number of black crystals of TOA[Au$_{25}$(PET)$_{18}$] could be observed at the bottom of the beaker.

Synthesis of Au(C≡C^{t}Bu)

50 mg of chloro(dimethylsulfanyl)gold(I) was added to 5 mL of acetone, 60 μL of 3,3-dimethyl-1-butyne, and 30.5 μL of triethylamine in a 20 mL round-bottomed flask and stirred in the dark for two hours. The mixed solution can be used directly for ligand exchange without purification.

Exchange of –C≡C^{t}Bu with TOA[Au$_{25}$(PET)$_{18}$]

Ligand exchange was performed by adding 1 mL of mixed solution containing Au(C≡C^{t}Bu) and 12 mg of TOA[Au$_{25}$(PET)$_{18}$] into 3 mL of dichloromethane in a 20 mL round-bottomed flask. The solution was stirred for three hours at room temperature in darkness. Then, the product was washed with methanol two times and extracted with DCM. The crude products dissolved in 2 mL of DCM were smeared on ten pieces of
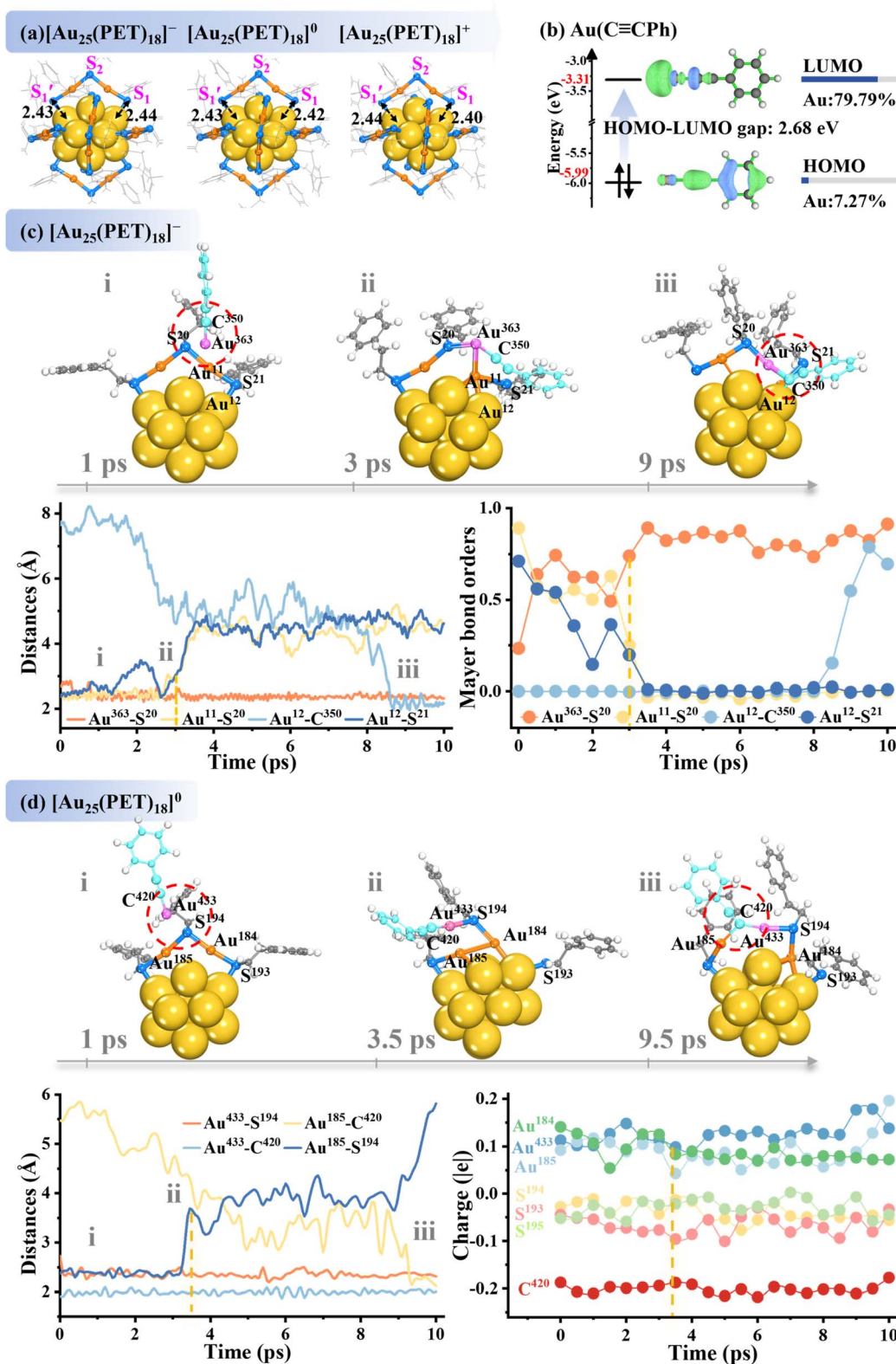
Fig. 1   (a) Structures of $[Au_{25}(PET)_{18}]^q$ clusters ($q = -1, 0, 1$; PET = 2-phenylethanethiol), where the surface Au–S bond lengths are inset. (b) Frontier orbitals of the Au(C≡CPh) fragment. (c) AIMD snapshots at 298 K depicting the key stages of Au(C≡CPh) ligand exchange on $[Au_{25}(PET)_{18}]^-$, displaying the bond length and Mayer bond order variations. (d) Snapshot structures, bond length dynamics, and CM5 charges for Au(C≡CPh) exchange on neutral $[Au_{25}(PET)_{18}]^0$. For clarity, only the Au_{13} core and one dimeric staple motif that reacts with the incoming Au(C≡CPh) ligand are shown in $[Au_{25}(PET)_{18}]^-$ (c) and $[Au_{25}(PET)_{18}]^0$ (d), while other staple motifs are omitted. Color code: C – sapphire (incoming ligand); Au – pink (incoming ligand); C – gray (Au_{25} cluster); S – blue; core Au – yellow (Au_{25} cluster); staple Au – orange (Au_{25} cluster); H – white.

preparative thin-layer chromatography (PTLC) plates (10 cm × 20 cm) and separated using an eluent (DCM/petroleum ether = 10/15 v/v). The brown band in the PTLC plate was cut off by using a knife and extracted by DCM. The DCM solution was dried by rotary evaporation for ESI-MS analysis.

Results and discussion

Ligand exchange between Au_{25} and $Au/Li(C{\equiv}CPh)$

To explore the dynamic exchange mechanism in thiol-capped Au_{25} NCs with alkynyl ligands, we used the well-characterized $[Au_{25}(PET)_{18}]^q$ ($q = -1$, 0, and 1) as a template (Fig. 1a) and introduced a series of alkynyl ligands (Scheme 1b) to study the ligand exchange process *via* AIMD simulations. We start with the negatively charged $[Au_{25}(PET)_{18}]^-$ as the parent cluster. Our initial simulations with the free phenylacetylene (HC≡CPh) as the incoming ligand did not induce any exchange on $[Au_{25}(PET)_{18}]^-$, even at an elevated temperature of 373 K (Fig. S1), where the cluster structure remained intact. The constrained AIMD (c-MD) simulations further revealed an extremely high energy barrier of 3.03 eV for the HC≡CPh-for-PET ligand displacement (Fig. S2b), affirming the robustness of Au–S coordination towards the incoming HC≡CPh ligand. Although the weak π-interactions were observed between the C≡C bond and the staple Au atoms, these interactions were insufficient to rival the robust Au–S bonds. In contrast,
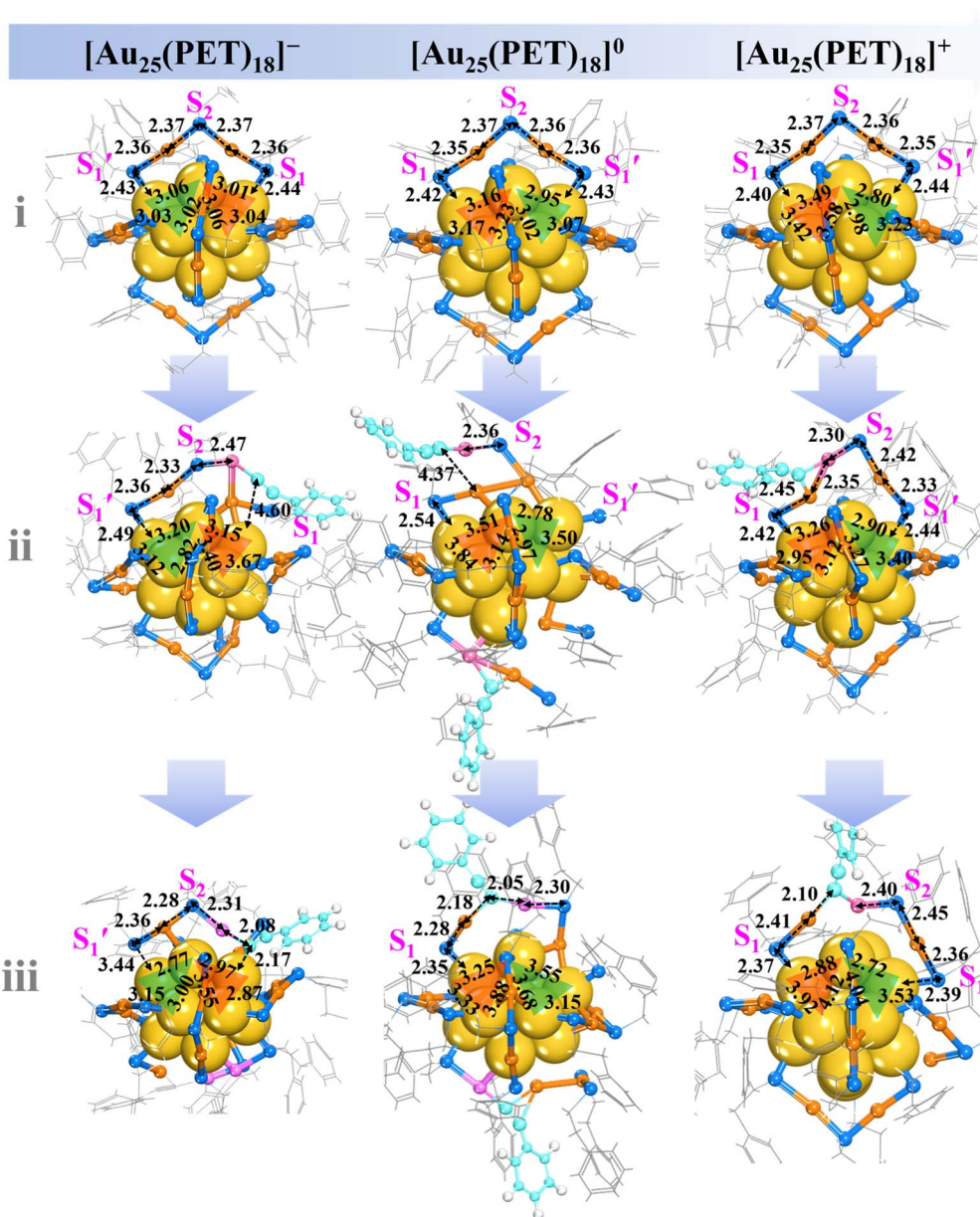

Fig. 2 The overall structural variation of $[Au_{25}(PET)_{18}]^-$, $[Au_{25}(PET)_{18}]^0$ and $[Au_{25}(PET)_{18}]^+$ NCs from stage (i) to stage (ii) and to stage (iii) during the 10 ps AIMD simulations at 298 K in the ligand exchange process. Color code: C – sapphire (incoming ligand); Au – pink (incoming ligand); C – gray (Au_{25} cluster); S – blue; core Au – yellow (Au_{25} cluster); staple Au – orange (Au_{25} cluster); H – white.

introducing alkynyl as the gold(I)–phenylacetylide complex (Au(C≡CPh)) enabled efficient ligand exchange on $[Au_{25}(PET)_{18}]^-$. Compared with free HC≡CPh, the Au–C σ-bond in Au(C≡CPh) has increased electron density, resulting in a reduction in LUMO energy primarily due to 79.79% contribution from the Au atom (Fig. 1b). This greatly narrows the HOMO–LUMO gap to 2.68 eV in Au(C≡CPh), as compared to 5.51 eV in HC≡CPh (Fig. S2a), enhancing the reactivity. Fig. 1c presents the AIMD snapshots at 298 K detailing the key stages in this exchange process, which displays the dynamic changes in bond lengths and Mayer bond order (MBO). Initially, a strong attraction forms between the active Au^{363} atom in Au(C≡CPh) and the apex S^{20} atom on the staple motif (stage (i)). This attraction leads to reinforcement of the $Au^{363}\cdots S^{20}$ interaction, evidenced by a reduced bond length (<3 Å) and an MBO of 0.74 within the first 1 ps (Fig. 1c). Concurrently, the staple Au^{11}–S^{20} bond weakens, as reflected by the dropping of its MBO to 0.51. At around 3 ps, a covalent bond forms between Au^{363} and S^{20} (MBO = 0.74), while the staple Au^{11}–S^{20} bond and the surface Au^{12}–S^{21} bond elongate to ~3 Å, with their MBOs falling to zero, marking a significant structural reconfiguration (stage (ii)). At around 9 ps, the C^{350} atom from the alkynyl C≡C group coordinates with the surface Au^{12} atom, forming a stable δ-bond interaction that completes the ligand exchange process (stage (iii); MBO = 0.70). This exchange process demonstrates a characteristic associative SN2-like mechanism,[30,61] in which both the incoming and outgoing ligands transiently coordinate with Au atoms, facilitating the smooth ligand substitution. The CM5 charge analysis (Fig. S3) captures the transient charge redistribution during the exchange reaction, showing temporary electron fluctuations as ligands exchange within the Au_{25} framework. This exchange culminates in a stable "S_1" regioisomer, characterized by [Au–SR] units being directly replaced with Au(C≡CPh) fragments (Fig. 1c). These findings underscore the critical role of Au^+ ions in driving the SN2-like ligand substitution and reveal the intricate dynamics of ligand exchange in metal clusters, highlighting the unique reactivity of Au(C≡CPh) complexes.

Moreover, it is well known that the charge state of metal NC could significantly modulate its electronic structure and, consequently, its reactivity.[62,63] Interestingly, Au_{25} NCs can readily interconvert their charged states between Au_{25}^- and Au_{25}^0 under mild conditions in the presence of oxygen or thiols.[62,64] However, the influence of charge state on the ligand-exchange mechanism in Au_{25} has not been clarified. To probe this, we performed the alkynyl-for-thiol exchange simulations on the neutral $[Au_{25}(PET)_{18}]^0$ NC. Intriguingly, different from the preferred "S_1" regioisomer in $[Au_{25}(PET)_{18}]^{-1}$, the "S_2" isomer emerged as the primary exchange product in $[Au_{25}(PET)_{18}]^0$ (Fig. 1d), suggesting a charge-mediated effect on the regioselectivity. In the neutral $[Au_{25}(PET)_{18}]^0$ NC, the Au^{433} atom in the Au(C≡CPh) complex moves closer to the apex S^{194} (3.50 Å, stage (i)), destabilizing the staple Au^{185}–S^{194} bond (2.81 Å) by drawing the electron density away from the S, which subsequently dissociated at around 3.5 ps (stage (ii)). In particular, this bond disruption allows the gradual formation of a covalent Au^{185}–C^{420} bond, progressively shortening from

4.37 Å to 2.18 Å as the electron density redistributes from the Au center to the C≡C group (stage (iii)). The formation of the Au^{185}–C^{420} bond not only stabilizes the incoming alkynyl ligand but also imposes significant steric strain on the adjacent [S^{194}–Au^{184}–S^{193}] unit. This dynamic interaction results in the displacement of the S_2R fragment and ultimately expels the sterically crowded [Au^{184}–S^{193}] unit, favoring the formation of the S_2 regioisomer as the major exchange product. Note that the symmetrical geometry of $[Au_{25}(PET)_{18}]^0$ always promotes selective substitution at the apex S_2 site, independent of the initial location of the incoming Au(C≡CPh) ligand (Fig. S4). Herein, the observed regioselectivity is attributed to the unique electronic properties of the Au–C≡C bond, characterized by the d–π* back-bonding between the occupied Au d orbitals and the π* orbitals of the C≡C bond. This interaction enhances the C≡C bond's reactivity, thereby promoting the ligand substitution. In addition, we also investigated the ligand exchange of Au(C≡CPh) with positively charged $[Au_{25}(SR)_{18}]^+$. Our simulations revealed that the Au(C≡CPh) ligand would favorably attack and insert into the staple Au–S(apex) bond, which forms an elongated and distorted trimeric [RS–Au–PhC≡C–Au–SR–Au–SR] motif, limiting effective alkynyl ligand replacement (Fig. S5). This interesting charge-dependent transformation demonstrates how the charge state modulates the exchange dynamics and regioselectivity in the alkynyl-for-thiolate exchange reaction. These insights underscore the great promise for using charge-state control to drive regioselective substitution in gold NCs with finely tuned reactivity and stability.

Fig. 2 summarizes the overall structural variation of $[Au_{25}(PET)_{18}]^-$, $[Au_{25}(PET)_{18}]^0$ and $[Au_{25}(PET)_{18}]^+$ NCs from stage (i) to stage (iii) during the ligand exchange process within the 10 ps AIMD simulations at 298 K. Note that the simulations were conducted by reacting one Au_{25} NC with 10 equivalents of Au(C≡CPh) molecules, and we observed that two Au(C≡CPh) ligands can exchange onto $[Au_{25}(PET)_{18}]^0$ in a pair of symmetrical staple motifs, while only one Au(C≡CPh) ligand is added onto $[Au_{25}(PET)_{18}]^-$ and $[Au_{25}(PET)_{18}]^+$. Noteworthily, the SR ligand replacement in Au_{25} NCs consistently occurs at the exposed Au_3 faces of the uncapped icosahedron, independent of the charge state (note that the icosahedra has 20 triangular faces in total, the formation of six staple motifs leaves eight Au_3 faces that are not capped, and herein only two of the adjacent Au_3 triangles are shown shaded in green and red, wherein the three surface Au–Au bond lengths are inset in each shaded triangle). As shown in Fig. 2, the change in the charge state of Au_{25}^q NCs has a minimal effect on the Au_{staple}–S bond lengths but significantly alters the Au_{core}–S bonding at the "S_1" position (stage (i)), which shortens as the cluster charge increases (from 2.44 Å in Au_{25}^- to 2.40 Å in Au_{25}^+). Furthermore, increasing the charge state elongates the Au–Au bonds within the Au_3 faces, particularly in the exposed "pockets" marked by the red Au_3 triangle close to the "S_1" position. The induced local strain as well as the longer Au_{core}–S bond thus offer enhanced flexibility and facilitate the reaction at the "S_1" position. Moreover, during the ligand exchange reaction, the icosahedral Au_{13} core undergoes considerable reconstruction (Fig. S6). Initially having an approximate D_{2h} symmetry, the stability of the icosahedron
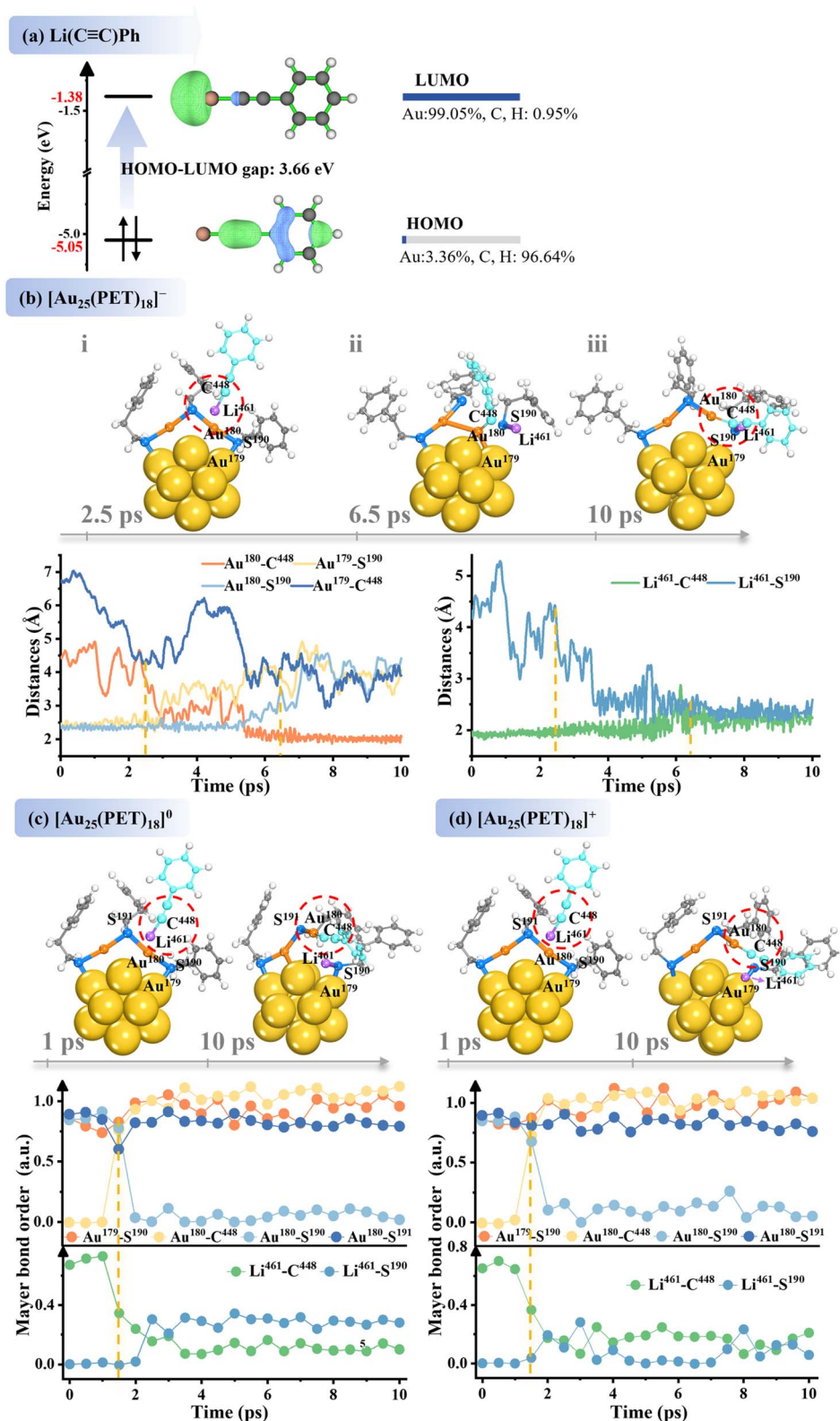
Fig. 3 (a) Frontier orbitals of the Li(C≡CPh) fragment. (b) AIMD snapshots depicting key stages of Li(C≡CPh) ligand exchange on $[Au_{25}(PET)_{18}]^-$, as well as the bond length variations during the 10 ps simulations at 298 K. The variation of Mayer bond order in ligand exchange of Li(C≡CPh) on $[Au_{25}(PET)_{18}]^0$ (c) and $[Au_{25}(PET)_{18}]^+$ (d) during the 10 ps AIMD simulations at 298 K, where the final snapshot structures are shown in the inset. The Li atom in the incoming ligand is colored in purple. Color code: C – sapphire (incoming ligand); C – gray (Au_{25} cluster); S – blue; core Au – yellow (Au_{25} cluster); staple Au – orange (Au_{25} cluster); Li – purple; H – white.
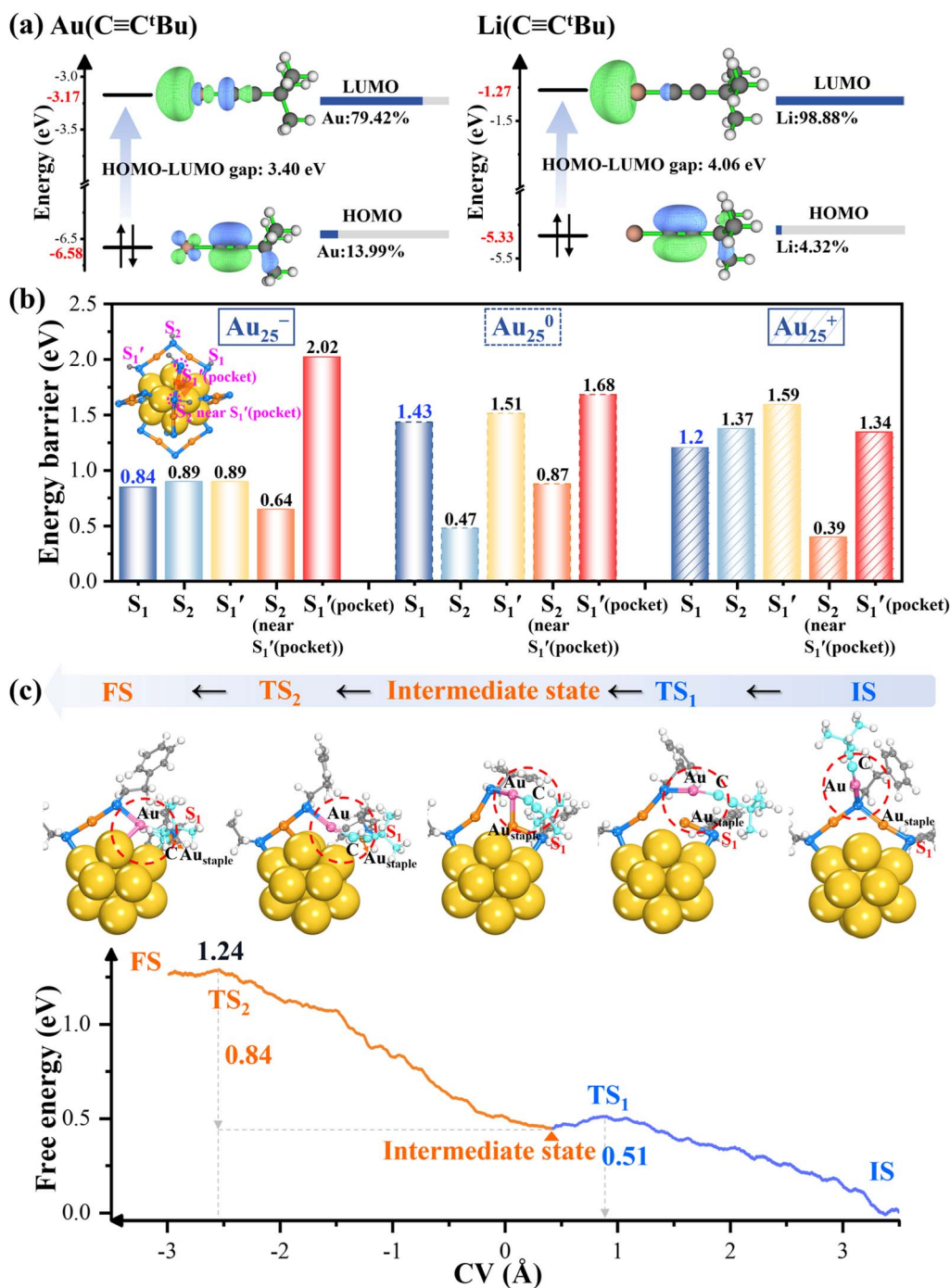
Fig. 4 (a) Frontier orbitals of Au(C≡C^{t}Bu) and Li(C≡C^{t}Bu) fragments. (b) Free energy barriers for the ligand exchange reaction between Au(C≡C^{t}Bu) and [Au$_{25}$(PET)$_{18}$]^q ($q = -1$, 0, and 1) at S$_1$, S$_2$, S$_1'$, S$_2$ (near S$_1'$(pocket)), and S$_1'$(pocket) sites during the c-MD simulations. (c) Reaction mechanism and free energy diagram for the Au(C≡C^{t}Bu) ligand exchange on [Au$_{25}$(PET)$_{18}$]$^-$ at the S$_1$ site. Color code: C – sapphire (incoming ligand); Au – pink (incoming ligand); C – -gray (Au$_{25}$ cluster); S – blue; core Au – yellow (Au$_{25}$ cluster); staple Au – orange (Au$_{25}$ cluster); H – white.

core is intensively sensitive to the ligand bonding modes.[43] Rigid alkynyl ligands like –C≡CPh would induce atomic rearrangement of surface atoms around the exchange site, which transiently destabilizes the core upon coexistence with alkynyl ligands until the stability is restored upon complete alkynyl integration (stage (iii)). In the anionic Au$_{25}^-$ NC, the shorter Au–

Au bonds on the surface of Au$_{13}$ core impart greater stability, with minimal structural deviation in the mono-alkynyl-coordinated cluster. In contrast, the neutral Au$_{25}^0$ NC shows slight distortion in the post-exchange process, while the cationic Au$_{25}^+$ NC experiences further amplified distortion in the Au$_{13}$ core. Obviously, as the cluster charge progresses from -1 to $+1$, the

charge-driven rearrangements increasingly influence the ligand exchange pathway, underscoring its critical role in controlling the structural stability and specificity in the substitution site.

Building on our above investigation of the exchange reaction between Au_{25} and $Au(C\equiv CPh)$, we further examined the exchange of lithium phenylacetylide ($Li(C\equiv CPh)$) on $Au_{25}(PET)_{18}$ to understand how the change in the metal center affects the exchange reaction dynamics. Lithium, with a smaller ionic radius (1.52 Å) and higher electropositivity (0.98), forms a significantly more ionic Li–C bond compared to the covalent Au–C bond in $Au(C\equiv CPh)$. This ionic character alters the electronic environment of the alkynyl group, reducing the electron delocalization and thereby increasing the HOMO and LUMO energies of the $C\equiv C$ bond (−5.05 and −1.38 eV, respectively, Fig. 3a), driven by a high contribution (99.05%) from Li in the LUMO, as compared to $Au(C\equiv CPh)$. The resulting electron-rich $C\equiv C$ bond displays greater nucleophilicity, enhancing its coordination ability with the Au site in the cluster's staple motif, facilitating a more efficient ligand exchange. In Fig. 3b, the –$C\equiv CPh$ moiety initially coordinates with the staple Au^{180} of $[Au_{25}(PET)_{18}]^-$, prompting the structural rearrangement that enhances the nucleophilic interaction. This coordination strengthens the Au^{180}–C^{448} bond, stabilizing at 2.5 Å around 2.5 ps, while concurrently the Li–C bond weakens to 2.0 Å, allowing the Li atom to approach S^{190}, which in turn induces steric and electronic strain that weakens the surface Au^{179}–S^{190} bond, extending it to 2.85 Å. At 6.5 ps (Fig. 3b, stage (ii)), the increased interaction between Au^{180} and C^{448} (2.07 Å; MBO = 0.86; Fig. S7) facilitates the dissociation of the staple Au^{180}–S^{190} bond, as indicated by the MBO reduction to 0.15. This bond reconfiguration induces the formation of a polar covalent Li–S bond with significant ionic character (2.51 Å; MBO = 0.32), anchoring the formed RS–Li complex to the cluster surface. Simultaneously, the Li–C bond weakens, as evidenced by its elongation (2.21 Å). This progression ultimately releases the –$C\equiv CPh$ moiety, allowing it to replace the original SR ligand and form the "S_1'" isomer (stage (iii), Fig. 3b). This exchange mechanism demonstrates that the ionic nature of the Li–C bond, in combination with the nucleophilic feature of the –$C\equiv CPh$ moiety, promote an efficient ligand exchange in $[Au_{25}(PET)_{18}]^-$.

In addition, similar to the case in $[Au_{25}(PET)_{18}]^-$, both $[Au_{25}(PET)_{18}]^0$ (Fig. 3c) and $[Au_{25}(PET)_{18}]^+$ (Fig. 3d) also preferably produce the exchange isomer at the "S_1'" site when interacting with the incoming $Li(C\equiv CPh)$ (Fig. S8 and S9). Notably, despite the greater MBO fluctuations in Au_{25}^+ indicating the higher structural sensitivity, the cluster's structural integrity remains stable across different charge states during the exchange process. Interestingly, the Li atom in $Li(C\equiv CPh)$ primarily serves as a mediator in the alkynyl-for-thiolate exchange, facilitating the exchange but without integrating into the cluster's structure. This may explain why the overall structural reorganization of Au_{25} is less pronounced than that in the exchange with $Au(C\equiv CPh)$. Overall, the ionic Li–C bond facilitates the dynamic adjustments, promoting the regioselective substitution with minimal steric hindrance. By comparison, the covalent Au–C bond in $Au(C\equiv CPh)$ stabilizes the interactions

with Au_{25} but restricts exchange flexibility, highlighting a key distinction in their reactivity. These findings illustrate that the metals in acetylide with distinct bonding characteristics (e.g., ionic versus covalent) can significantly affect the ligand exchange dynamics. Leveraging these differences opens up new avenues for designing functionalized gold NCs with tailored properties, enabling precise control over cluster stability and reactivity.

Ligand exchange between Au_{25} and $Au/Li(C\equiv C^tBu)$

Furthermore, based on the insights from the –$C\equiv CPh$ exchange, we additionally considered the bulky tert-butyl group –$C\equiv C^tBu$ to examine how the increased steric hindrance impacts the ligand exchange in Au_{25} NCs. The tert-butyl group introduces considerable steric effects and unique electronic characteristics, providing an opportunity to understand how the presence of larger substituents modifies the exchange behavior. As shown in Fig. S10a, $HC\equiv C^tBu$ has a significantly wider HOMO–LUMO gap of 8.73 eV compared to 5.51 eV in $HC\equiv CPh$, primarily due to the electron localization. Incorporating Au or Li into the –$C\equiv C^tBu$ group notably reduces the LUMO energy (Fig. 4a), resulting in a narrower HOMO–LUMO gap of 3.40 eV and 4.06 eV, respectively. Compared to their Au/Li$(C\equiv CPh)$ analogues (2.68 and 3.66 eV), the bulkier Au/Li$(C\equiv C^tBu)$ complexes demonstrate an increased HOMO–LUMO gap, underscoring the combined effects of metal incorporation and steric bulkiness in fine-tuning the electronic properties.

We first assessed the exchange feasibility of the $HC\equiv C^tBu$ ligand. From Fig. S10b, our c-MD simulations at 298 K revealed a high free energy barrier of 3.48 eV for –$C\equiv C^tBu$ binding with the staple Au in $[Au_{25}(PET)_{18}]^-$ to realize the "S_1'" exchange, indicating the significant challenge of the $HC\equiv C^tBu$ exchange. In the case of $Au(C\equiv C^tBu)$, the unconstrained AIMD simulations around 10 ps at 298 K in various Au_{25} charge states (−1, 0, and +1) showed that the incoming $Au(C\equiv C^tBu)$ ligand would be adsorbed and bonded to the S atom of the original thiolate ligand, but no noticeable ligand exchange was observed (Fig. S11). Note that this finding is drastically distinct from that of the prior $Au(C\equiv CPh)$ ligand where the $Au(C\equiv CPh)$-for-thiolate exchange occurs spontaneously in the unconstrained 10 ps AIMD simulations. This suggests that the incorporation of the bulkier (–$C\equiv C^tBu$) group would greatly decelerate the exchange reaction kinetics. To capture the activation barrier for the ligand exchange reaction, we then employed the c-MD free energy calculations to analyze the formation of an exchange isomer in Au_{25} when it reacts with the bulkier $Au(C\equiv C^tBu)$ complex. Herein, we investigated three potential exchange sites: S_1, S_2 and S_1', where S_1 is located within the pocket region, as described previously. Note that our above studies on the $Au(C\equiv CPh)$ exchange have highlighted the critical role of S_1 site in the ligand exchange, particularly within the pocket region. Based on these findings, we also considered additional sites: the S_1'(pocket) position within the pocket and the S_2 position adjacent to S_1'(pocket), hereafter referred to as 'S_2 (near S_1'(pocket))' (Fig. 4b, inset). This broader analysis provides

a more comprehensive view of ligand exchange dynamics in and around the pocket site, as revealed by the c-MD simulations. The calculated energy barriers for the ligand exchange at the five designated positions—S_1, S_2, S_1', S_2 (near S_1'(pocket)), and S_1'(pocket)—are presented in Fig. 4b. Note that the substitution at the S_2 and S_2 (near S_1'(pocket)) positions is hindered by the steric effects (Fig. S12–S14), resulting in incomplete exchange despite the relatively lower barriers. In contrast, the S_1 position consistently exhibits the lowest energy barriers across all the charge states (0.84 eV for Au_{25}^-, 1.43 eV for Au_{25}^0, and 1.2 eV for Au_{25}^+), highlighting the energetic preference of ligand exchange at the S_1 site. The higher barriers and significant steric effects at other positions (e.g., S_2 and S_1') limit their accessibility, making S_1 isomer as the most favorable exchange product across all the charge states (Fig. S12–S14). Consequently, the bulkier Au(C≡C^{t}Bu) incoming ligand exhibits a pronounced regioselectivity toward the S_1 position near the pocket, while Au(C≡CPh) shows charge-dependent regioselectivity.

Moreover, analogous to the Au(C≡CPh)-for-thiolate exchange observed in the unconstrained MD simulations, the Au(C≡C^{t}Bu)-for-thiolate exchange follows a two-step mechanism. In the first step, the bulkier Au(C≡C^{t}Bu) ligand adsorbs at the S site. The second step is determined by the ligand's binding mode: coordination to the Au_{13} core leads to the formation of S_1 or S_1' isomers, while binding to the Au_{staple} results in S_2 or S_2 (near S_1'(pocket)) isomers (Fig. S12–S14). The energy barriers shown in Fig. 4b correspond to three distinct pathways: (i) formation of the S_1 isomer, (ii) formation of the S_2 and S_2 (near S_1'(pocket)) isomers, and (iii) formation of the S_1' and S_1'(pocket) isomers, as illustrated in Fig. 4c and S15. Taking the formation of the S_1 isomer on the Au_{25}^- cluster as an example, the S–Au bond first cleaves with a low energy barrier (≤0.57 eV), facilitating stable adsorption of the –C≡C^{t}Bu ligand onto the staple Au moiety (Fig. 4c). In the subsequent step (the rate-determining step), the –C≡C^{t}Bu moiety forms a C–Au α-bond with the Au_{13} core, requiring a higher energy barrier (≥0.84 eV) to complete the exchange. However, the moderate overall barriers (≤1.5 eV) indicate that both steps are experimentally accessible. Notably, the rate-limiting formation of the C–Au α-bond occurs most readily in the $[Au_{25}(PET)_{18}]^-$ cluster (0.84 eV), followed by $[Au_{25}(PET)_{18}]^+$ (1.20 eV) and $[Au_{25}(PET)_{18}]^0$ (1.43 eV) (Fig. 4b). Additionally, the exchange mechanisms for the S_2 (near S_1'(pocket)) and S_1'(pocket) isomer formations (ii and iii) on $[Au_{25}(PET)_{18}]^-$ are depicted in Fig. S15, along with the corresponding key geometric structures.

Fig. S16 illustrates the structural evolution of $[Au_{25}(PET)_{18}]^-$, $[Au_{25}(PET)_{18}]^0$ and $[Au_{25}(PET)_{18}]^+$ NCs from the initial state (IS) through an intermediate state to the final state (FS) during the ligand exchange via c-MD simulations. The results confirm that the SR replacement is restricted to the exposed "pockets" marked by the red Au_3 triangle, regardless of the charge state. Variations in the charge state primarily affect the local bonding environment at the Au_{core}–S_1 and Au_{core} – S_1'(pocket) positions (IS). Specifically, as the charge of Au_{25}^q NCs increases, the Au_{core}–S_1 bond elongates from 2.36 Å in Au_{25}^- to 2.47 Å in Au_{25}^+, while the Au_{core} – S_1'(pocket) bond extends from 2.39 Å to 2.43 Å. These changes are accompanied by the slight elongation of

Au–Au bonds within the Au_3 face within the pocket region (red triangle, Fig. S16). The Au_{core}–S bond at "S_1" is consistently longer than that at "S_1'(pocket)", inducing tensile strain localized at the S_1 site. This strain enhances the dynamic flexibility of the S_1 site, weakening the Au_{core}–S covalent interaction and collectively facilitating ligand exchange with the sterically demanding Au(C≡C^{t}Bu) ligands. Notably, a slight reconstruction of the Au_{13} core occurs during the exchange process, which is caused by the surface atom rearrangements driven by the bulky alkynyl ligands temporarily destabilizing the core structure. This instability is mitigated once the –C≡C^{t}Bu moiety fully integrates into the cluster framework in the final state (FS). Note that the higher charge states amplify these structural distortions, reducing the bond length uniformity across the cluster. These findings also highlight the significant impact of charge states on the ligand exchange at the single-ligand level.

Furthermore, in contrast to Au(C≡C^{t}Bu), the interaction of Li(C≡C^{t}Bu) with $[Au_{25}(PET)_{18}]^0$, shown in Fig. 5a, reveals a facile spontaneous ligand exchange during the unconstrained AIMD simulations at 298 K. In fact, the strong ionic C–Li interaction increases the nucleophilicity of the alkynyl group, promoting its adsorption onto the staple Au^6 motif and facilitating the formation of the Au–C α-bond between the –C≡C^{t}Bu group and the Au^6 site (2.19 Å, (ii)) at around 2.2 ps. Concurrently, the Li ion gradually coordinates with the S_1' atom (∼3 Å), and as the Au^6–C^{366} and Li–S^{16} bonds strengthen, the Au^6–S^{16} bond progressively weakens and eventually breaks (3.5 Å, (iii)) at around 10 ps, completing the exchange process. To further confirm that the –C≡C^{t}Bu group can adsorb onto the Au_{13} core, we present a free energy calculation for the subsequent S_1' isomer formation on $[Au_{25}(PET)_{18}]^0$, following the exchange with 10 equivalents of Li(C≡C^{t}Bu) molecules via c-MD simulations (Fig. 5b). The low barrier (0.64 eV) indicates that the exchanged alkynyl group can readily coordinate with the unsaturated Au atom on the icosahedron surface, stabilizing the Au_{13} core and forming newly mixed-ligand capped Au_{25}^0 NCs. In the case of the negatively charged $[Au_{25}(PET)_{18}]^-$ cluster, the c-MD simulations (Fig. 5c) reveal the initially spontaneous adsorption of the –C≡C^{t}Bu moiety onto the staple Au site with a minimal energy barrier (0.05 eV, Fig. S17). This is followed by the ligand exchange at the S_1' position, which occurs with a lower energy barrier (1.08 eV) compared to the S_1 site (1.57 eV, Fig. S18), confirming the preferred regioselectivity of the S_1 isomer. For the positively charged $[Au_{25}(PET)_{18}]^+$ cluster, the exchange barrier at the S_1' position is 0.94 eV (Fig. 5d); nevertheless, the final state (FS) exhibits greater geometric distortion and instability in the icosahedral Au_{13} core. These findings highlight that the incorporation of Li into the –C≡C^{t}Bu moiety ensures 100% selective formation of the S_1' isomer. The exchange with the Li(C≡C^{t}Bu) group to form the S_1' isomer is energetically more facile on $[Au_{25}(SR)_{18}]^0$, followed by $[Au_{25}(PET)_{18}]^-$ and $[Au_{25}(PET)_{18}]^+$ NCs. These results underscore the potential to engineer metal clusters with tailored steric and electronic properties, offering precise control over the ligand exchange efficiency and reactivity.
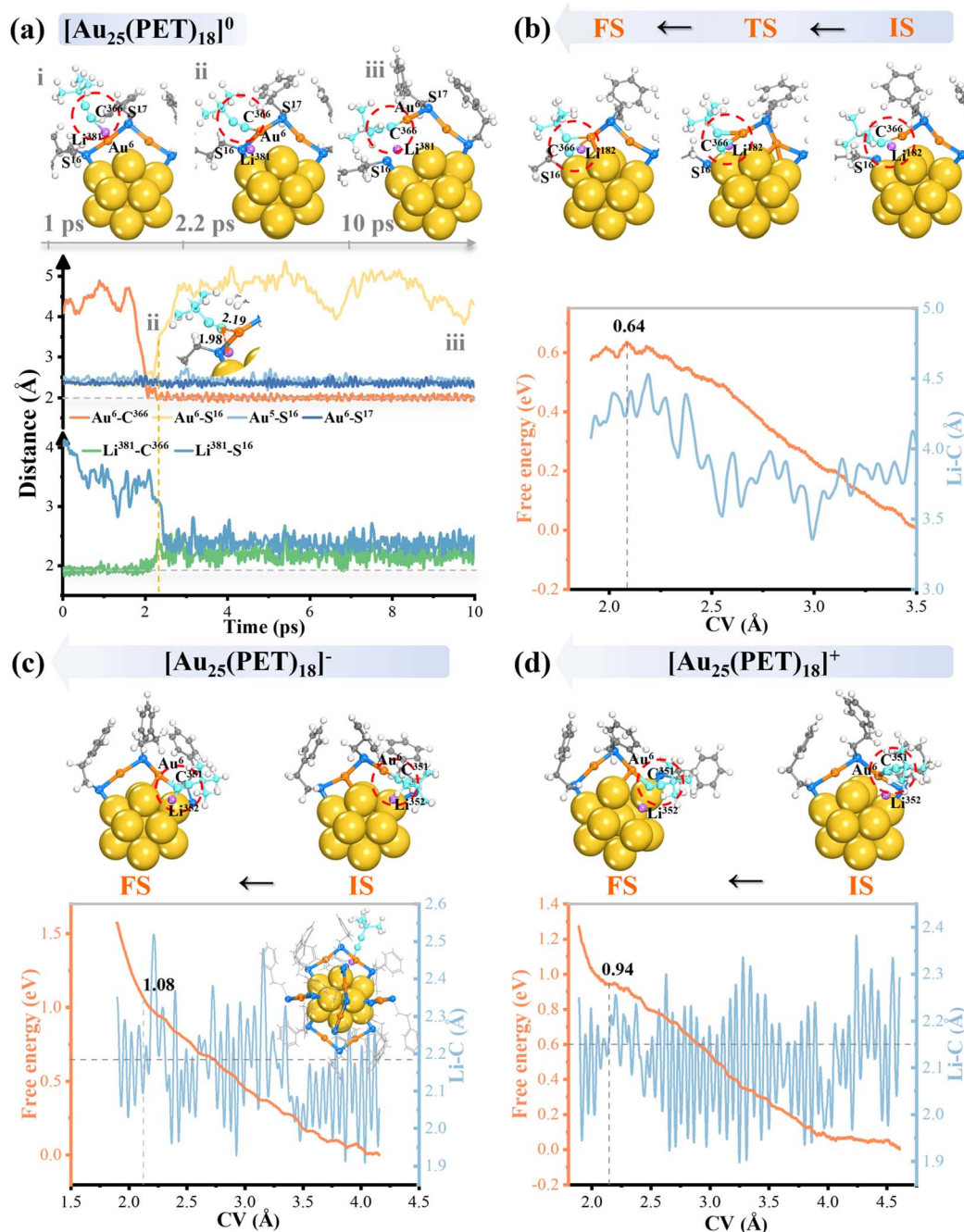
Fig. 5 (a) AIMD snapshots depicting key stages of Li(C≡C^{t}Bu) ligand exchange on [Au$_{25}$(PET)$_{18}$]^0, along with the bond length variations during the 10 ps unconstrained AIMD simulations at 298 K. (b) Mechanistic pathway and free energy diagram of subsequent S$_1^'$ isomer formation on the [Au$_{25}$(PET)$_{18}$]^0 cluster upon exchange with 10 equivalents of Li(C≡C^{t}Bu) molecules. Mechanistic step and free energy diagram of S$_1^'$ isomer formation during Li(C≡C^{t}Bu) exchange with (c) [Au$_{25}$(PET)$_{18}$]$^-$ and (d) [Au$_{25}$(PET)$_{18}$]$^+$ clusters. Color code: C – sapphire (incoming ligand); C – gray (Au$_{25}$ cluster); S – blue; core Au – yellow (Au$_{25}$ cluster); staple Au – orange (Au$_{25}$ cluster); Li – purple; H – white.

Furthermore, to confirm the applicability of AIMD in simpler systems (such as mononuclear complexes) and different reaction systems, we simulated the PET-to-TBBT (TBBT = 4-*tert*-butylbenzenethiolate) conversion in Au$_{25}$. As shown in Fig. S19, AIMD simulations of this process successfully identified a high energy barrier of 1.91 eV. The reaction proceeds through a concerted attack by H and S of TBBT on the S and Au$_{staple}$ of

Au$_{25}$, respectively (IS), leading to TBBT adsorption onto Au$_{staple}$ (intermediate state), ultimately leading to PET dissociation (FS). Crucially, the PET-to-TBBT conversion offers a structurally less complex and core-stable way compared to the original SR-to-alkynyl exchange. These simulations confirm that AIMD can effectively capture the key dynamic features (such as energy barriers) in ligand displacement processes.

Experimental validation

In order to verify the alkynyl-for-thiolate exchange on the Au_{25} clusters, $[Au_{25}(PET)_{18}]^-$ was used as the starting material, and the ligand exchange products were detected by electrospray ionization mass spectroscopy (ESI-MS) measurements. TOA $[Au_{25}(PET)_{18}]$ (TOA$[Au_{25}]$, TOA = tetraoctylammonium) was synthesized in accordance with the previous report.[60] The ligand-exchange reaction of $[Au_{25}]^-$ with $-C{\equiv}C^tBu$ was performed by adding excess $Au(C{\equiv}C^tBu)$ to a dichloromethane (DCM) solution of TOA$[Au_{25}]$ at room temperature in darkness for 3 hours. After the ligand exchange process, the 695 nm peak in the UV/vis/NIR absorption spectra of $[Au_{25}]^-$ red-shifted to 715 nm (Fig. S20). In positive mode ESI-MS, three discrete peaks in the range m/z 3650–3750 can be discerned at m/z 3662.67, 3690.67 and 3718.65, respectively (Fig. 6a). These complexes can be assigned to $[Au_{25}(PET)_{18-x}(C{\equiv}C^tBu)_x + 2Cs]^{2+}$ with the x values of 6, 5, and 4, respectively. Within the range m/z 7160 to 7340 , another three peaks are observed at m/z 7190.14, 7247.10 and 7303.05, respectively (Fig. 6b). The three products can be designated as $[Au_{25}(PET)_{18-x}(C{\equiv}C^tBu)_x + Cs]^+$ with x values of 6, 5, and 4, respectively. The ESI-MS data of the two different valence products indicate that 4, 5 and 6 PET ligands have been exchanged for $-C{\equiv}C^tBu$ on $[Au_{25}]^-$ during the process of ligand exchange. The isotopic pattern also matched well with $[Au_{25}(PET)_{13}(C{\equiv}C^tBu)_5 + 2Cs]^{2+}$ and $[Au_{25}(PET)_{13}(C{\equiv}C^tBu)_5 + Cs]^+$ (Fig. 6c and d). The remaining isotopic patterns matched well with the simulations (Fig. S21 and S22), and $Au_{25}(PET)_{18-x}(C{\equiv}C^tBu)_x$ can be further auto-oxidized to $[Au_{25}(PET)_{18-x}(C{\equiv}C^tBu)_x]^+$. As shown in Fig. S23, three discrete

peaks in the range m/z 7040 and 7181 can be discerned at m/z 7058.14, 7114.22 and 7170.26, respectively. These complexes can be assigned to $[Au_{25}(PET)_{18-x}(C{\equiv}C^tBu)_x]^+$ with x values of 6, 5, and 4, respectively. Altogether, these pieces of experimental evidence clearly show that it is possible to exchange the PET ligand with the new $-C{\equiv}C^tBu$ ligand on the $[Au_{25}(PET)_{18}]^-$ nanocluster under ambient conditions.

For the synthesis of $Au(C{\equiv}C^tBu)$, it is essential to retain the acetone solvent and avoid its loss. Removal of acetone would prevent the complete re-dissolution of $Au(C{\equiv}C^tBu)$ and subsequent ligand exchange. Furthermore, during the ligand exchange reaction between $Au(C{\equiv}C^tBu)$ and TOA$[Au_{25}(PET)_{18}]$, significant insoluble precipitation was observed following PTLC separation after solvent removal. These observations collectively demonstrate that the solvent is essential for maintaining the stability of both $Au(C{\equiv}C^tBu)$ and the ligand-exchanged product $Au_{25}(PET)_{18-x}(C{\equiv}C^tBu)_x$. Besides $Au(C{\equiv}C^tBu)$, $Au(C{\equiv}CPh)$ has also been shown to undergo ligand exchange with TOA $[Au_{25}(PET)_{18}]$.[41] Unfortunately, the product has not been successfully identified so far. Due to the difficult access to $Li(C{\equiv}CR)$ in our lab, the related ligand exchange process was only theoretically investigated.

It is noted that our experimental optimization established that 20–40 ligand equivalents are required for $Au(C{\equiv}C^tBu)$-for-PET exchange in the Au_{25}^- cluster, indicating tolerance to ligand concentration within this range. Our AIMD simulations employed ligand concentrations of 10–40 equivalents, encompassing the core experimental range (20–40 equivalents) while extending to 10 equivalents to investigate concentration-dependent trends. Simulations revealed consistent ligand
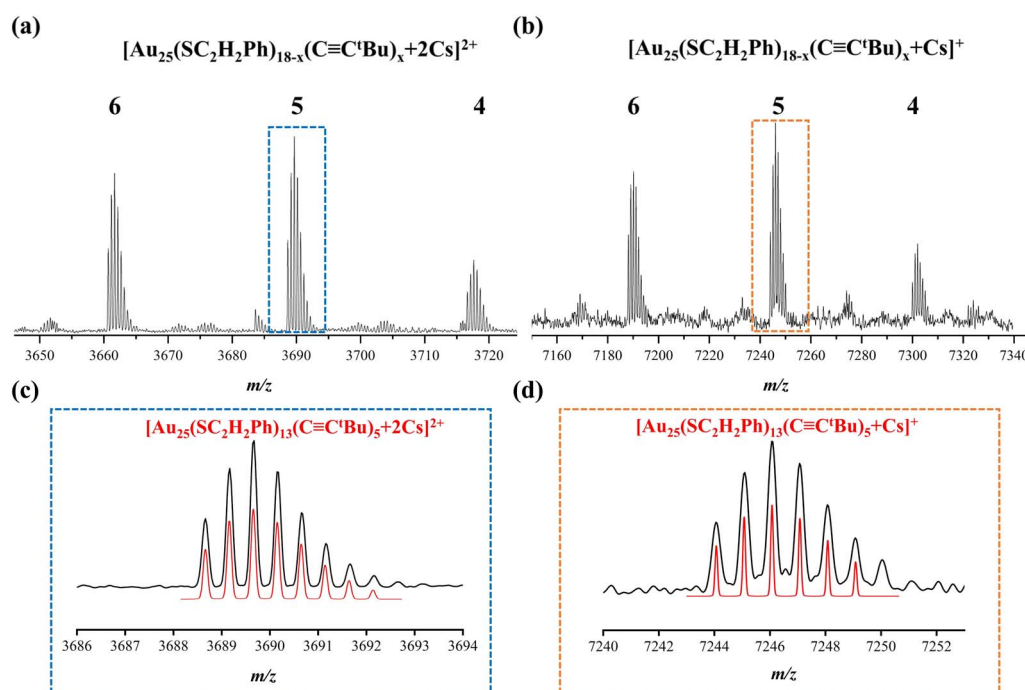
Fig. 6 Positive-ion mode ESI-MS spectra of the product clusters (a) $[Au_{25}(PET)_{18-x}(C{\equiv}C^tBu)_x + 2Cs]^{2+}$ and (b) $[Au_{25}(PET)_{18-x}(C{\equiv}C^tBu)_x + Cs]^+$ after the ligand exchange of PET with $-C{\equiv}C^tBu$, and x represents the number of exchanged ligands. (c and d) Experimental (dark lines) and simulated (red lines) isotopic pattern comparisons of $[Au_{25}(PET)_{13}(C{\equiv}C^tBu)_5 + 2Cs]^{2+}$ and $[Au_{25}(PET)_{13}(C{\equiv}C^tBu)_5 + Cs]^+$, respectively.

binding efficiency, reaction pathways, and exchange outcomes across 10–40 equivalents. This demonstrates system insensitivity to ligand concentration within this window and aligns with experiments showing that concentration primarily governs exchange kinetics—not the fundamental mechanism. Thus, our simulation design directly corresponds to experimental conditions, with the extended range validating result reliability under experimental concentrations. Moreover, computational constraints limited our simulations to single Au(C≡C^{t}Bu)-for-PET exchange in Au_{25}^-, yet experimental findings reveal up to six ligand substitutions. To resolve this discrepancy, we propose a possible stepwise substitution mechanism supported by bond length and Bader charge analyses (Fig. S24). The $Au_{25}(PET)_{18}$ framework features six dimeric [RS–Au(I)–SR–Au(I)–SR] units surrounding the icosahedral Au_{13} core, yielding three possible distinct regioisomers (S_1, S_2, and S_1') upon ligand exchange. Structural characterization and Bader charge analysis reveal persistently maintained dual S–Au bonds and a more positive charge localized at the central S_2 site in mono-substituted clusters, conferring exchange resistance at this position. While following a single Au(C≡C^{t}Bu)-for-PET exchange in Au_{25}^-, five S sites (red) exhibit elongated S–Au bonds (Au–S >2.45 Å) and acquire a negative charge. These activated sites originating from distinct $Au_2(SR)_3$ units demonstrate greater attraction toward Au atoms in the incoming Au(C≡C^{t}Bu) ligands. Collectively, the progressive structural and electronic modifications induced by initial substitution facilitate subsequent exchanges, thereby accounting for the observed multi-ligand substitution pathway.

Discussion

Electronic effects

Our above results on the kinetics of –C≡CR-for-thiolate exchange in $[Au_{25}(PET)_{18}]^q$ NCs (q = −1, 0, and +1) unveil a highly innovative and unique mechanism governing the reactivity and selectivity. Our findings highlight the decisive role of metal–alkynyl complexes (*e.g.*, Au(C≡CPh) and Li(C≡CPh)) in driving the alkynyl-for-thiolate exchange, a metathesis reaction involving thiolate and alkynyl groups. The metal fundamentally alters the electronic properties of the –C≡CR group, significantly enhancing their reactivity compared to the rigid HC≡CR molecule. The incorporation of Au (r_{Au} = 1.36 Å) or Li (r_{Li} = 1.28 Å) enhances the spatial flexibility of the Au–C (1.926 Å) and Li–C (1.896 Å) bonds, while the increased electron-donating capability of C≡C moiety facilitates efficient electronic reorganization, thereby facilitating the ligand exchange. The Electron Localization Function (ELF) analysis confirms this mechanism, where the electron localization around the C≡C moiety of HC≡CPh and HC≡C^{t}Bu is concentrated and rigid, limiting the interactions with $Au_{25}(SR)_{18}$ (Fig. S25a and b). By contrast, Au incorporation into the –C≡CR group induces significant electron redistribution (Fig. S25c and d), reducing electron localization around the Au–C bond and creating an asymmetric electron distribution along the C≡C bond. The Localization Molecular Orbital (LMO) analysis (Fig. S26) further reveals that this redistribution originates from the d–π* interactions, involving back-donation of

the occupied Au d-orbital electrons into the π* orbitals of the C≡C moiety. This back-donation not only strengthens the covalent character of the Au–C bond but also redistributes and polarizes the π*-electron density of the alkynyl group, thereby significantly enhancing its reactivity. Frontier molecular orbital analysis (Fig. 1b and 4a) further supports this mechanism, with the LUMO dominated by the Au contributions (79.79% and 79.42%), highlighting the Au-driven electronic polarization and structural activation of the alkynyl ligand. Moreover, for the Li–alkynyl complex (Fig. S25e and f), the ELF analysis confirms the predominantly ionic nature of the Li–C bond with limited charge transfer. Nevertheless, this ionic interaction intensifies the π*-electron density around the C≡C bond, boosting the alkynyl nucleophilicity, as reflected in the LMO analysis (Fig. S26). Intriguingly, while Li does not directly participate in the exchange reaction, its capacity to polarize the –C≡CR electronic structure plays a critical role for the ligand exchange. Together, these findings establish that the distinct yet complementary roles of Au and Li in alkynyl-to-thiolate exchange arise from their distinct contribution to the electronic structure, with Au driving the covalent activation and Li inducing the ionic polarization.

Steric hindrance effects

Steric hindrance critically governs the dynamics and regioselectivity of the ligand exchange. The bulkier HC≡C^{t}Bu with a kinetic diameter of 6.99 Å, imposes greater spatial constraints than HC≡CPh (4.03 Å, Fig. S27). The Interaction Region Indicator (IRI) analysis reveals pronounced steric clashes between –C≡C^{t}Bu and PET ligands on Au_{25}, restricting the binding-site accessibility and slowing the exchange kinetics (Fig. S28). The compact –C≡CPh experiences minimal steric interference, forming weak cluster–surface interactions. Taking Au(C≡CR)-for-thiolate exchange as an example, this accessibility permits selective exchange at the S_1 or S_2 positions depending on the charge state, while the bulky –C≡C^{t}Bu limits the exchange process only to the less hindered S_1 site across all the charge states. These comparative analyses demonstrate how the ligand bulkiness dictates the exchange efficiency and positional selectivity through steric modulation of binding-site accessibility and surface interaction dynamics.

Charge state of Au_{25} clusters

The charge-state variations in Au_{25} NCs modulate the structural stability, which in turn regulates the ligand binding dynamics. These effects stem from the quantum size properties of Au_{25} NCs, which govern their electronic and absorptive behavior.[43] The anionic $[Au_{25}(PET)_{18}]^-$ demonstrates the maximal stability, minimizing the reorganization during interaction with Au/Li(C≡CR) (Fig. 2 and S16). Variations in charge states induce the structural adjustments in Au_{core}–S and Au–Au bond lengths within the pocket region of $Au_{25}(PET)_{18}$, which directly influence the regioselectivity. For Au(C≡CPh) with lower steric hindrance, the stable Au_{25}^- NC selectively substitutes the [Au–S_1R] unit to form the S_1 isomer. The neutral Au_{25}^0 undergoes moderate structural rearrangement, compressing the [Au–S_1R]

unit to yield the S_2 isomer. Whereas the instability of the Au_{13} core in Au_{25}^+ induces significant structural distortion and impedes the exchange. For the bulkier $-C\equiv C^tBu$ ligand, the $Au_{core}-S$ bond lengths provide a steric advantage to the less hindered S_1 position. Notably, the $Li(C\equiv CR)$ complexes exhibit the charge-state-independent reactivity, achieving nearly 100% S_1' selectivity due to the ionic Li–C bond's insensitivity to the electrostatic modulation. These results reflect the exchange regioselectivity as a synergistic interplay of steric effects and charge-driven structural dynamics.

While this work focuses on PET-protected $Au_{25}(SR)_{18}^-$ clusters, the revealed alkynyl-for-thiolate exchange mechanism may exhibit broader physicochemical implications. Given the shared structural principles governing noble metal nanoclusters, we anticipate its potential applicability to other systems featuring comparable metallic cores and bonding motifs. For homologous gold clusters such as $Au_{38}(PET)_{24}$[65] which contains six dimeric $Au_2(SR)_3$ staple motifs, structurally analogous to Au_{25}, mechanistic commonalities in the ligand exchange process are highly probable. Similarly, Ag_{25} (e.g., $[Ag_{25}(SPhMe_2)_{18}]^-$)[66] and their alloyed analogues (e.g., Au_xAg_{25-x})[67–69] possess analogous Au_{25}-like core–shell structures. Notably, alloying-induced core rigidity may reduce exchange kinetics while enhancing structural stability during ligand exchange. Furthermore, variations in the ligand environment, such as thiolate chain length or functional groups, could critically modulate exchange efficiency through steric or electronic effects.[9] Longer thiolate chains are expected to impose greater steric hindrance, while different functional groups (e.g., $-NHCs$[70,71] and $-COOH$[72,73]) may significantly alter electronic donation/withdrawal effects, thereby influencing the affinity for alkynyl ligands. We emphasize that validating these hypotheses requires integrated approaches combining computational modeling, atomically precise structural characterization, and system-specific in situ spectroscopy techniques. This delineates clear and necessary avenues for future research.

Conclusion

In summary, we have performed extensive AIMD simulations to reveal the alkynyl-for-thiolate exchange mechanism in the atomically precise $Au_{25}(SR)_{18}$ prototype cluster. By systematically probing the electronic and steric effects of the exchange ligand as well as the charge state of Au_{25}^q ($q = -1$, 0, and $+1$) NCs, we identify that the electronic characteristics of the alkynyl ligands in the metal–alkynyl complex (e.g., $Au(C\equiv CPh)$ or $Li(C\equiv CPh)$) play the decisive role in determining the nucleophilicity and initiating the exchange reactions. In the dynamic exchange process with the $Au(C\equiv CR)$ complex, the anionic $[Au_{25}(SR)_{18}]^-$ favors to form the S_1 isomer, whereas the S_2 isomer is the dominant product when the neutral $Au_{25}(SR)_{18}$ is used as the precursor. Differently, the sterically bulky $Au(C\equiv C^tBu)$ complex preferentially targets the S_1 position, attributed to the steric hindrance with PET ligands that restricts its access to the binding sites. Interestingly, the alkynyl-for-thiolate exchange ensures 100% selective formation of the S_1' isomer when using the lithium–alkynyl complex ($Li(C\equiv CR)$) as

the incoming ligand. Our experimental validation further confirms the successful alkynyl-for-thiolate exchange on the model cluster $[Au_{25}(PET)_{18}]^-$, where up to 6 PET ligands can be substituted by the alkynyl $-C\equiv C^tBu$ ligands. Overall, these findings greatly deepen our understanding of the exchange reaction between thiolates and alkynyl ligands, leading to the insightful design guidelines for the creation of novel gold nanoclusters with new chemical functions and interface properties.

Author contributions

Yuping Chen: conceptualization, data curation, formal analysis, investigation, methodology, writing – original draft; Guoqing Bian: investigation, methodology; Zhikun Wu: supervision, resources, writing – review & editing; Qing Tang: conceptualization, supervision, resources, writing – review & editing.

Conflicts of interest

The authors declare no conflict of interests.

Data availability

The data supporting this article have been included as part of the SI. Supplementary information: Additional simulation models, reaction coordinates for constrained AIMD simulations, free energy profiles, HOMO and LUMO, CM5 atomic charges, Electron Localization Function (ELF) maps, Localized Molecular Orbitals (LMOs), Interaction Region Indicator (IRI) plots, and UV/vis/NIR absorption spectra. See DOI: https://doi.org/10.1039/d5sc04701c.

Acknowledgements

References

1 R. Jin, C. Zeng, M. Zhou and Y. Chen, Atomically Precise Colloidal Metal Nanoclusters and Nanoparticles: Fundamentals and Opportunities, Chem. Rev., 2016, 116(18), 10346–10413.

2 Y. Zhu, H. Qian, B. A. Drake and R. Jin, Atomically Precise $Au_{25}(SR)_{18}$ Nanoparticles as Catalysts for the Selective Hydrogenation of α, β-Unsaturated Ketones and Aldehydes, Angew. Chem., Int. Ed., 2010, 7(49), 1295–1298.

3 S. Li, D. Alfonso, A. V. Nagarajan, S. D. House, J. C. Yang, D. R. Kauffman, G. Mpourmpakis and R. Jin, Monopalladium Substitution in Gold Nanoclusters

Enhances CO_2 Electroreduction Activity and Selectivity, *ACS Catal.*, 2020, **10**(20), 12011–12016.

4 W. Jing, H. Shen, R. Qin, Q. Wu, K. Liu and N. Zheng, Surface and Interface Coordination Chemistry Learned from Model Heterogeneous Metal Nanocatalysts: From Atomically Dispersed Catalysts to Atomically Precise Clusters, *Chem. Rev.*, 2022, **123**(9), 5948–6002.

5 B. Zhang, J. Chen, Y. Cao, O. J. H. Chai and J. Xie, Ligand Design in Ligand-Protected Gold Nanoclusters, *Small*, 2021, **17**(27), 2004381.

6 M. Cui, Y. Shi, X. Ma, Q. Li, L. Chen, L. Zhang, J. Wu, H. Yu and M. Zhu, The Pivotal Radical Intermediate $[Au_{21}(SR)_{15}]^+$ in the Ligand-Exchange-Induced Size-Reduction of $[Au_{23}(SR)_{16}]^-$ to $Au_{16}(SR)_{12}$, *ACS Nano*, 2024, **18**(8), 6591–6599.

7 V. Truttmann, C. Herzig, I. Illes, A. Limbeck, E. Pittenauer, M. Stöger-Pollach, G. Allmaier, T. Bürgi, N. Barrabés and G. Rupprechter, Ligand Engineering of Immobilized Nanoclusters on Surfaces: Ligand Exchange Reactions with Supported $Au_{11}(PPh_3)_7Br_3$, *Nanoscale*, 2020, **12**(24), 12809–12816.

8 Y. Cao, V. Fung, Q. Yao, T. Chen, S. Zang, D.-e. Jiang and J. Xie, Control of Single-Ligand Chemistry on Thiolated Au_{25} Nanoclusters, *Nat. Commun.*, 2020, **11**(1), 5498.

9 W. Suzuki, R. Takahata, Y. Chiga, S. Kikkawa, S. Yamazoe, Y. Mizuhata, N. Tokitoh and T. Teranishi, Control over Ligand-Exchange Positions of Thiolate-Protected Gold Nanoclusters using Steric Repulsion of Protecting Ligands, *J. Am. Chem. Soc.*, 2022, **144**(27), 12310–12320.

10 G. Salassa, A. Sels, F. Mancin and T. Burgi, Dynamic Nature of Thiolate Monolayer in $Au_{25}(SR)_{18}$ Nanoclusters, *ACS Nano*, 2017, **11**(12), 12609–12614.

11 Y. Zeng, S. Havenridge, M. Gharib, A. Baksi, K. L. D. M. Weerawardene, A. R. Ziefuß, C. Strelow, C. Rehbock, A. Mews, S. Barcikowski, *et al.*, Impact of Ligands on Structural and Optical Properties of Ag_{29} Nanoclusters, *J. Am. Chem. Soc.*, 2021, **143**(25), 9405–9414.

12 J. Dong, Z. Gan, W. Gu, Q. You, Y. Zhao, J. Zha, J. Li, H. Deng, N. Yan and Z. Wu, Synthesizing Photoluminescent $Au_{28}(SCH_2Ph\text{-}^tBu)_{22}$ Nanoclusters with Structural Features by Using a Combined Method, *Angew. Chem., Int. Ed.*, 2021, **133**(33), 18076–18080.

13 H. Yao, Chiral Ligand-Protected Gold Nanoclusters: Considering the Optical Activity from a Viewpoint of Ligand Dissymmetric Field, *Prog. Nat. Sci.*, 2016, **26**(5), 428–439.

14 C. A. Hosier and C. J. Ackerson, Regiochemistry of Thiolate for Selenolate Ligand Exchange on Gold Clusters, *J. Am. Chem. Soc.*, 2019, **141**(1), 309–314.

15 Y. Li, T. Higaki, X. Du and R. Jin, Chirality and Surface Bonding Correlation in Atomically Precise Metal Nanoclusters, *Adv. Mater.*, 2020, **32**(41), 1905488.

16 L. Cseh and G. H. Mehl, The Design and Investigation of Room Temperature Thermotropic Nematic Gold Nanoparticles, *J. Am. Chem. Soc.*, 2006, **128**(41), 13376–13377.

17 Q. Yao, X. Yuan, Y. Yu, Y. Yu, J. Xie and J. Y. Lee, Introducing Amphiphilicity to Noble Metal Nanoclusters via Phase-Transfer Driven Ion-Pairing Reaction, *J. Am. Chem. Soc.*, 2015, **137**(5), 2128–2136.

18 W. Ndugire and M. Yan, Synthesis and Solution Isomerization of Water-Soluble Au_9 Nanoclusters Prepared by Nuclearity Conversion of $[Au_{11}(PPh_3)_8Cl_2]Cl$, *Nanoscale*, 2021, **13**(39), 16809–16817.

19 H. Shen, Z. Xu, M. S. A. Hazer, Q. Wu, J. Peng, R. Qin, S. Malola, B. K. Teo, H. Häkkinen and N. Zheng, Surface Coordination of Multiple Ligands Endows N-Heterocyclic Carbene-Stabilized Gold Nanoclusters with High Robustness and Surface Reactivity, *Angew. Chem., Int. Ed.*, 2021, **60**(7), 3752–3758.

20 Z. Luo, K. Zheng and J. Xie, Engineering Ultrasmall Water-Soluble Gold and Silver Nanoclusters for Biomedical Applications, *Chem. Commun.*, 2014, **50**(40), 5143–5155.

21 A. Retnakumari, S. Setua, D. Menon, P. Ravindran, H. Muhammed, T. Pradeep, S. Nair and M. Koyakutty, Molecular-Receptor-Specific, Non-Toxic, Near-Infrared-Emitting Au Cluster-Protein Nanoconjugates for Targeted Cancer Imaging, *Nat. Nanotechnol.*, 2009, **21**(5), 055103.

22 M. Sera, S. Hossain, S. Yoshikawa, K. Takemae, A. Ikeda, T. Tanaka, T. Kosaka, Y. Niihori, T. Kawawaki and Y. Negishi, Atomically Precise $Au_{24}Pt$ (thiolate)$_{12}$(dithiolate)$_3$ Nanoclusters with Excellent Electrocatalytic Hydrogen Evolution Reactivity, *J. Am. Chem. Soc.*, 2024, **146**(43), 29684–29693.

23 T. Lahtinen, E. Hulkko, K. Sokołowska, T.-R. Tero, V. Saarnio, J. Lindgren, M. Pettersson, H. Häkkinen and L. Lehtovaara, Covalently Linked Multimers of Gold Nanoclusters $Au_{102}(p\text{-}MBA)_{44}$ and $Au_{\sim250}(p\text{-}MBA)_n$, *Nanoscale*, 2016, **8**(44), 18665–18674.

24 Q. Zhu, X. Huang, Y. Zeng, K. Sun, L. Zhou, Y. Liu, L. Luo, S. Tian and X. Sun, Controllable Synthesis and Electrocatalytic Applications of Atomically Precise Gold Nanoclusters, *Nanoscale Adv.*, 2021, **3**(22), 6330–6341.

25 J. Zhao, A. Ziarati, A. Rosspeintner, Y. Wang and T. Bürgi, Engineering Ligand Chemistry on Au_{25} Nanoclusters: from Unique Ligand Addition to Precisely Controllable Ligand Exchange, *Chem. Sci.*, 2023, **14**(28), 7665–7674.

26 Y. Chen, C. Liu, Q. Tang, C. Zeng, T. Higaki, A. Das, D.-e. Jiang, N. L. Rosi and R. Jin, Isomerism in $Au_{28}(SR)_{20}$ Nanocluster and Stable Structures, *J. Am. Chem. Soc.*, 2016, **138**(5), 1482–1485.

27 Y. Negishi, H. Horihata, A. Ebina, S. Miyajima, M. Nakamoto, A. Ikeda, T. Kawawaki and S. Hossain, Selective Formation of $[Au_{23}(SPh^tBu)_{17}]^0$, $[Au_{26}Pd(SPh^tBu)_{20}]^0$ and $[Au_{24}Pt(SC_2H_4Ph)_7(SPh^tBu)_{11}]^0$ by Controlling Ligand-exchange Reaction, *Chem. Sci.*, 2022, **13**(19), 5546–5556.

28 P. D. Jadzinsky, G. Calero, C. J. Ackerson, D. A. Bushnell and R. D. Kornberg, Structure of a Thiol Monolayer-Protected Gold Nanoparticle at 1.1 Å Resolution, *Science*, 2007, **318**(5849), 430–433.

29 M. W. Heaven, A. Dass, P. S. White, K. M. Holt and R. W. Murray, Crystal Structure of the Gold Nanoparticle

[N(C_8H_{17})$_4$][Au_{25}(SCH_2CH_2Ph)$_{18}$], *J. Am. Chem. Soc.*, 2008, **130**(12), 3754–3755.

30 M. J. Hostetler, A. C. Templeton and R. W. Murray, Dynamics of Place-Exchange Reactions on Monolayer-Protected Gold Cluster Molecules, *Langmuir*, 1999, **15**(11), 3782–3789.

31 H. Xiang, H. Yan, J. Liu, R. Cheng, C.-Q. Xu, J. Li and C. Yao, Identifying the Real Chemistry of the Synthesis and Reversible Transformation of AuCd Bimetallic Clusters, *J. Am. Chem. Soc.*, 2022, **144**(31), 14248–14257.

32 X. Ma, Y. Tang, G. Ma, L. Qin and Z. Tang, Controllable Synthesis and Formation Mechanism Study of Homoleptic Alkynyl-Protected Au Nanoclusters: Recent Advances, Grand Challenges, and Great Opportunities, *Nanoscale*, 2021, **13**(2), 602–614.

33 P. Maity, H. Tsunoyama, M. Yamauchi, S. Xie and T. Tsukuda, Organogold Clusters Protected by Phenylacetylene, *J. Am. Chem. Soc.*, 2011, **133**(50), 20123–20125.

34 M. Sugiuchi, Y. Shichibu, T. Nakanishi, Y. Hasegawa and K. Konishi, Cluster–π Electronic Interaction in a Superatomic Au_{13} Cluster Bearing σ-Bonded Acetylide Ligands, *Chem. Commun.*, 2015, **51**(70), 13519–13522.

35 X.-K. Wan, Q. Tang, S.-F. Yuan, D.-e. Jiang and Q.-M. Wang, Au_{19} Nanocluster Featuring a V-Shaped Alkynyl–Gold Motif, *J. Am. Chem. Soc.*, 2015, **137**(2), 652–655.

36 Z. Lei, X.-K. Wan, S.-F. Yuan, Z.-J. Guan and Q.-M. Wang, Alkynyl Approach toward the Protection of Metal Nanoclusters, *Acc. Chem. Res.*, 2018, **51**(10), 2465–2474.

37 X. K. Wan, Z. J. Guan and Q. M. Wang, Homoleptic Alkynyl-Protected Gold Nanoclusters: Au_{44}(PhC≡C)$_{28}$ and Au_{36}(PhC≡C)$_{24}$, *Angew. Chem., Int. Ed.*, 2017, **56**(38), 11494–11497.

38 J.-J. Li, Z.-J. Guan, Z. Lei, F. Hu and Q.-M. Wang, Same Magic Number but Different Arrangement: Alkynyl-Protected Au_{25} with D_3 Symmetry, *Angew. Chem., Int. Ed.*, 2019, **58**(4), 1083–1087.

39 X.-K. Wan, J.-Q. Wang, Z.-A. Nan and Q.-M. Wang, Ligand Effects in Catalysis by Atomically Precise Gold Nanoclusters, *Sci. Adv.*, 2017, **3**(10), e1701823.

40 X. Li, S. Takano and T. Tsukuda, Ligand Effects on the Hydrogen Evolution Reaction Catalyzed by Au_{13} and Pt@Au_{12}: Alkynyl *vs.* Thiolate, *J. Phys. Chem. C*, 2021, **125**(42), 23226–23230.

41 C. A. Hosier, I. D. Anderson and C. J. Ackerson, Acetylide-for-Thiolate and Thiolate-for-Acetylide Exchange on Gold Nanoclusters, *Nanoscale*, 2020, **12**(11), 6239–6242.

42 K. Isozaki, K. Iseri, R. Saito, K. Ueda and M. Nakamura, Dual Catalysis of Gold Nanoclusters: Photocatalytic Cross-Dehydrogenative Coupling by Cooperation of Superatomic Core and Molecularly Modified Staples, *Angew. Chem., Int. Ed.*, 2024, **136**(2), e202312135.

43 M. Zhu, C. M. Aikens, F. J. Hollander, G. C. Schatz and R. Jin, Correlating the Crystal Structure of a Thiol-Protected Au_{25} Cluster and Optical Properties, *J. Am. Chem. Soc.*, 2008, **130**(18), 5883–5885.

44 J. VandeVondele, M. Krack, F. Mohamed, M. Parrinello, T. Chassaing and J. Hutter, Quickstep: Fast and Accurate Density Functional Calculations using a Mixed Gaussian and Plane Waves Approach, *Comput. Phys. Commun.*, 2005, **167**(2), 103–128.

45 J. P. Perdew, K. Burke and M. Ernzerhof, Generalized Gradient Approximation Made Simple, *Phys. Rev. Lett.*, 1996, **77**(18), 3865.

46 C. Hartwigsen, S. Gœdecker and J. Hutter, Relativistic Separable Dual-Space Gaussian Pseudopotentials from H to Rn, *Phys. Rev. B:Condens. Matter Mater. Phys.*, 1998, **58**(7), 3641.

47 S. Grimme, S. Ehrlich and L. Goerigk, Effect of the Damping Function in Dispersion Corrected Density Functional Theory, *J. Comput. Chem.*, 2011, **32**(7), 1456–1465.

48 G. J. Martyna, M. L. Klein and M. Tuckerman, Nosé–Hoover Chains: The Canonical Ensemble via Continuous Dynamics, *J. Chem. Phys.*, 1992, **97**(4), 2635–2643.

49 E. A. Carter, G. Ciccotti, J. T. Hynes and R. Kapral, Constrained Reaction Coordinate Dynamics for the Simulation of Rare Events, *Chem. Phys. Lett.*, 1989, **156**(5), 472–477.

50 M. Sprik and G. Ciccotti, Free Energy from Constrained Molecular Dynamics, *J. Chem. Phys.*, 1998, **109**(18), 7737–7744.

51 M. Frisch, G. Trucks, H. Schlegel, G. Scuseria, M. Robb, J. Cheeseman, G. Scalmani, V. Barone, G. Petersson and H. Nakatsuji, *Gaussian 16, Revision A. 03*, Gaussian, Inc., Wallingford, CT, 2016.

52 S. Huzinaga, J. Andzelm, E. Radzio-Andzelm, Y. Sakai, H. Tatewaki and M. Klobukowski, *Gaussian Basis Sets for Molecular Calculations*, Elsevier, 2012.

53 D. Andrae, U. Häußermann, M. Dolg, H. Stoll and H. Preuß, Energy-Adjusted ab Initio Pseudopotentials for the Second and Third Row Transition Elements, *Theor. Chim. Acta*, 1990, **77**(2), 123–141.

54 S. Grimme, J. Antony, S. Ehrlich and H. Krieg, A Consistent and Accurate ab Initio Parametrization of Density Functional Dispersion Correction (DFT-D) for the 94 Elements H-Pu, *J. Chem. Phys.*, 2010, **132**(15), 154104.

55 J. Stevenson, B. Sorenson, V. H. Subramaniam, J. Raiford, P. P. Khlyabich, Y.-L. Loo and P. Clancy, Mayer Bond Order as a Metric of Complexation Effectiveness in Lead Halide Perovskite Solutions, *Chem. Mater.*, 2017, **29**(6), 2435–2444.

56 I. Mayer, Charge, Bond Order and Valence in the ab Initio SCF Theory, *Chem. Phys. Lett.*, 1983, **97**(3), 270–274.

57 I. Mayer, Bond Order and Valence: Relations to Mulliken's Population Analysis, *Int. J. Quantum Chem.*, 1984, **26**(1), 151–154.

58 T. Lu and F. Chen, Multiwfn: A Multifunctional Wavefunction Analyzer, *J. Comput. Chem.*, 2012, **33**(5), 580–592.

59 Z. Lei, J. J. Li, X. K. Wan, W. H. Zhang and Q. M. Wang, Isolation and Total Structure Determination of an All-Alkynyl-Protected Gold Nanocluster Au_{144}, *Angew. Chem., Int. Ed.*, 2018, **57**(28), 8639–8643.

60 L. Liao, S. Zhou, Y. Dai, L. Liu, C. Yao, C. Fu, J. Yang and Z. Wu, Mono-Mercury Doping of Au_{25} and the HOMO/

LUMO Energies Evaluation Employing Differential Pulse Voltammetry, *J. Am. Chem. Soc.*, 2015, **137**(30), 9511–9514.

61 C. L. Heinecke, T. W. Ni, S. Malola, V. Makinen, O. A. Wong, H. Hakkinen and C. J. Ackerson, Structural and Theoretical Basis for Ligand Exchange on Thiolate Monolayer Protected Gold Nanoclusters, *J. Am. Chem. Soc.*, 2012, **134**(32), 13316–13322.

62 M. Zhu, C. M. Aikens, M. P. Hendrich, R. Gupta, H. Qian, G. C. Schatz and R. Jin, Reversible Switching of Magnetism in Thiolate-Protected Au_{25} Superatoms, *J. Am. Chem. Soc.*, 2009, **131**(7), 2490–2492.

63 S. Antonello, N. V. Perera, M. Ruzzi, J. A. Gascón and F. Maran, Interplay of Charge State, Lability, and Magnetism in the Molecule-like $Au_{25}(SR)_{18}$ Cluster, *J. Am. Chem. Soc.*, 2013, **135**(41), 15585–15594.

64 M. Zhu, W. T. Eckenhoff, T. Pintauer and R. Jin, Conversion of Anionic $[Au_{25}(SCH_2CH_2Ph)_{18}]^-$ Cluster to Charge Neutral Cluster via Air Oxidation, *J. Phys. Chem. C*, 2008, **112**(37), 14221–14224.

65 H. Qian, W. T. Eckenhoff, Y. Zhu, T. Pintauer and R. Jin, Total Structure Determination of Thiolate-Protected Au_{38} Nanoparticles, *J. Am. Chem. Soc.*, 2010, **132**(24), 8280–8281.

66 C. P. Joshi, M. S. Bootharaju, M. J. Alhilaly and O. M. Bakr, $[Ag_{25}(SR)_{18}]^-$: The "Golden" Silver Nanoparticle, *J. Am. Chem. Soc.*, 2015, **137**(36), 11578–11581.

67 L. He, Z. Gan, N. Xia, L. Liao and Z. Wu, Alternating Array Stacking of $Ag_{26}Au$ and $Ag_{24}Au$ Nanoclusters, *Angew. Chem., Int. Ed.*, 2019, **131**(29), 10002–10006.

68 D. Liu, W. Du, S. Chen, X. Kang, A. Chen, Y. Zhen, S. Jin, D. Hu, S. Wang and M. Zhu, Interdependence between nanoclusters $AuAg_{24}$ and Au_2Ag_{41}, *Nat. Commun.*, 2021, **12**(1), 778.

69 X. Liu, J. Yuan, C. Yao, J. Chen, L. Li, X. Bao, J. Yang and Z. Wu, Crystal and Solution Photoluminescence of $MAg_{24}(SR)_{18}$ (M = Ag/Pd/Pt/Au) Nanoclusters and Some Implications for the Photoluminescence Mechanisms, *J. Phys. Chem. C*, 2017, **121**(25), 13848–13853.

70 H. Shen, Z. Xu, M. S. A. Hazer, Q. Wu, J. Peng, R. Qin, S. Malola, B. K. Teo, H. Häkkinen and N. Zheng, Surface Coordination of Multiple Ligands Endows N-Heterocyclic Carbene-Stabilized Gold Nanoclusters with High Robustness and Surface Reactivity, *Angew. Chem., Int. Ed.*, 2021, **133**(7), 3796–3802.

71 M. R. Narouz, K. M. Osten, P. J. Unsworth, R. W. Man, K. Salorinne, S. Takano, R. Tomihara, S. Kaappa, S. Malola and C.-T. Dinh, N-Heterocyclic Carbene-Functionalized Magic-Number Gold Nanoclusters, *Nat. Chem.*, 2019, **11**(5), 419–425.

72 W.-D. Tian, W.-D. Si, S. Havenridge, C. Zhang, Z. Wang, C. M. Aikens, C.-H. Tung and D. Sun, Biomimetic Crystallization for Long-Pursued –COOH-Functionalized Gold Nanocluster with Near-Infrared Phosphorescence, *Sci. Bull.*, 2024, **69**(1), 40–48.

73 S. M. Han, M. Park, J. Kim and D. Lee, Boosting the Electroreduction of CO_2 to CO by Ligand Engineering of Gold Nanoclusters, *Angew. Chem., Int. Ed.*, 2024, **63**(31), e202404387.